A&A, 708, A295 (2026)
https://doi.org/10.1051/0004-6361/202556122

Astronomy & Astrophysics

The NIKA2 cosmological legacy survey at 2 mm: Catalogs, colors, redshift distributions, and implications for deep surveys

M. Béthermin[1,⋆], G. Lagache[2], C. Carvajal-Bohorquez[2], R. Adam[3], P. Ade[4], H. Ajeddig[5], S. Amarantidis[6], P. André[5], H. Aussel[5], A. Beelen[2], A. Benoît[7], S. Berta[9], L. J. Bing[8], A. Bongiovanni[6], J. Bounmy[10], O. Bourrion[10], M. Calvo[7], A. Catalano[10], D. Chérouvrier[10], M. De Petris[11], F.-X. Désert[12], S. Doyle[4], E. F. C. Driessen[9], G. Ejlali[13], A. Ferragamo[11], A. Gomez[14], J. Goupy[7], C. Hanser[15], S. Katsioli[16,17], F. Kéruzoré[18], C. Kramer[9], B. Ladjelate[6], S. Leclercq[9], J.-F. Lestrade[19], J. F. Macías-Pérez[10], S. C. Madden[5], A. Maury[20,21,5], F. Mayet[10], A. Monfardini[7], A. Moyer-Anin[10], M. Muñoz-Echeverría[22], I. Myserlis[6], A. Paliwal[23], L. Perotto[10], G. Pisano[11], N. Ponthieu[12], V. Revéret[5], A. J. Rigby[24], A. Ritacco[10], H. Roussel[25], F. Ruppin[26], M. Sánchez-Portal[6], S. Savorgnano[10], K. Schuster[9], A. Sievers[6], C. Tucker[4], and R. Zylka[9]

(Affiliations can be found after the references)

Received 26 June 2025 / Accepted 28 January 2026

ABSTRACT

Aims. Millimeter (mm) galaxy surveys are particularly effective in detecting dusty star-forming galaxies at high redshift. While such observations are typically conducted at ∼1 mm, various authors have suggested over the last 20 years that 2 mm observations may be better suited for selecting sources at even higher redshifts. In this work, we use the unprecedented 2 mm data from the NIKA2 Cosmological Legacy Survey (N2CLS), together with the simulated infrared dusty extragalactic sky (SIDES), to study and interpret the statistical properties of galaxies selected at this wavelength.

Methods. We used the N2CLS robust sample (95% purity) at 2 mm (∼18 arcsec resolution), which contains 25 sources in the deep GOODS-N field (159 arcmin^2, 0.047 mJy/beam RMS) and 90 sources in the wide COSMOS field (1130 arcmin^2, 0.09 mJy/beam RMS). The sources were matched with the N2CLS 1.2 mm sources, ancillary 850 µm sources, and redshift catalogs to study the colors and redshift distributions. We also produced end-to-end simulations based on SIDES and the observed N2CLS detector timelines to interpret the data.

Results. We found a mean $S_{2\,mm}/S_{1.2\,mm}$ color of 0.222 ± 0.008 with a standard deviation of 0.070 ± 0.010, mainly caused by resolution and source extraction effects according to the SIDES simulation. We measured a mean redshift of 3.6 ± 0.3 in GOODS-N, which is marginally higher than the expectations from SIDES (2.9 ± 0.2) because of an overdensity at $z \sim 5.2$, and 3.2 ± 0.2 in COSMOS, which is identical to that obtained in SIDES. We also show that the observed $S_{2\,mm}/S_{1.2\,mm}$ colors exhibit a weak dependence with redshift but a large dispersion, which limits its efficiency with respect to selecting high-z sources. We compared the measured fluxes of 2 mm sources detected by both the N2CLS and the Ex-MORA surveys. The results only agree if we take into account the impact of the bandwidth, source blending, and source size. Finally, we studied the eight 2 mm sources that had not been detected at 1.2 mm and found that two of them are radiogalaxies and one is a $z \sim 2$ galaxy, while the remaining six (all in COSMOS) are compatible with the expected number of spurious detections. Consequently, the N2CLS survey shows no evidence of any exotic dusty galaxy population with either very cold dust or at very high redshift, which would only be detectable at 2 mm. Using SIDES, we show that 2 mm samples have a higher mean redshift compared to 1.2 mm because they miss dusty galaxies around cosmic noon ($z \sim 2$). Finally, we discuss the efficiency of single-dish and interferometric blind surveys to build samples of high-z dusty galaxies.

Key words. surveys – galaxies: high-redshift – galaxies: star formation – submillimeter: galaxies

1. Introduction

Since the discovery of high-redshift bright submillimeter (submm) galaxies (e.g., Smail et al. 1997; Hughes et al. 1998; Blain et al. 2002; Chapman et al. 2003), the (sub)mm atmospheric window is the prime wavelength range to probe dusty star-forming systems in the high-z Universe ($z > 2$; see, e.g., Casey et al. 2014 and Hodge & da Cunha 2020 for reviews). Indeed, the peak of cold dust emission in the far-infrared (FIR, ∼80 µm) tracing obscured star formation is shifted to the submm windows by the redshift. The observed submm flux from galaxies at higher redshifts comes from rest-frame wavelengths closer to their peak of emission, compensating for the increasing luminosity distance and leading to an almost constant flux-versus-luminosity ratio at $z \gtrsim 2$ (e.g., Blain et al. 2002; Lagache et al. 2004). This effect is commonly referred to as the negative K-correction.

Observations have unveiled a numerous population of these submm galaxies that pose a challenge to galaxy evolution models, which struggle to produce enough objects with such high star formation rates in the early Universe (e.g., Baugh et al. 2005; Lovell et al. 2021; Hayward et al. 2021; Kumar et al. 2025). The Atacama large millimeter array (ALMA) showed that massive dusty galaxies are already present up to $z \sim 7$ (e.g., Strandet et al. 2017; Fudamoto et al. 2021). Several surveys have found that the obscured star formation density is already on the same order of magnitude as the unobscured one at $z \sim 5$ (e.g., Gruppioni et al. 2020; Zavala et al. 2021; Khusanova et al. 2021; Barrufet et al. 2023). Because of their high dust content, which absorbs a large

⋆ Corresponding author:
matthieu.bethermin@astro.unistra.fr

fraction of the light produced by their stars and re-emits it in the rest-frame FIR, dusty galaxies are very faint in the optical (e.g., Wang et al. 2019; Talia et al. 2021), but very bright in the observed (sub)mm.

While the first surveys were performed at 850 µm by the submm common-user bolometer array (SCUBA, Holland et al. 1999), other instruments on single-dish telescopes were developed to probe longer wavelengths[1] such as Bolocam (Laurent et al. 2005), AzTEC (e.g., Scott et al. 2012), or MAMBO (Lindner et al. 2011) at 1.1/1.2 mm, and GISMO (Staguhn et al. 2014; Magnelli et al. 2019) at 2 mm. In addition, a population of very bright sources at 1.4 mm magnified by gravitational lensing was found by the south pole telescope (SPT, Vieira et al. 2013, see also Lestrade et al. 2010 about an earlier single detection with MAMBO). Finally, ALMA offers the capacity to perform interferometric surveys through large mosaics of pointings and blind photometric surveys have been performed at 1 mm (e.g., Dunlop et al. 2017; Franco et al. 2018) and 2 mm (e.g., Casey et al. 2021; Long et al. 2024). The survey performed at longer wavelengths found sources at a higher average redshift (e.g., Simpson et al. 2014; Weiß et al. 2013; Staguhn et al. 2014; Casey et al. 2021; Cowie et al. 2023). This effect can easily be modeled considering the combination of the different (sub)mm flux versus redshift relation at different wavelengths (Zavala et al. 2014), the strong evolution of the dust luminosity function, and the impact of lensing at high flux (Béthermin et al. 2015a).

Performing deep surveys at longer wavelengths may appear an effective strategy for maximizing the number of high-redshift detections. However, things are more complex than they seem. At 2 mm, dusty galaxies even up to $z \sim 7$ are observed in the Rayleigh-Jeans regime with a flux density decreasing steeply with increasing wavelength. If the survey sensitivity is not significantly better than at shorter wavelengths, this could lead to fewer detections even at high redshift. However, surveys at 2 mm could be potentially powerful tools for detecting hypothetical rare dusty objects at very high redshifts. They could also be combined with shorter wavelength surveys to identify follow-up targets at high redshift (e.g., Casey et al. 2019; Cooper et al. 2022; Cowie et al. 2023) or with a very cold apparent dust temperature (e.g., Jin et al. 2022; Bing et al. 2024).

The new IRAM KIDS array (NIKA2, Monfardini et al. 2014; Calvo et al. 2016; Bourrion et al. 2016) was installed on the IRAM 30-meter telescope in October 2015 (Adam et al. 2018; Perotto et al. 2020) and can observe its circular 6.5 arcmin-diameter field of view simultaneously at 1.2 and 2 mm. Thanks to its combined high sensitivity and large field of view, NIKA2 is particularly efficient to perform blind surveys at these two wavelengths. The NIKA2 cosmological legacy survey (N2CLS) observed the GOODS-N and COSMOS fields. It provides both an unprecedented statistical sample of 2 mm sources and an unique opportunity to combine them with their 1.2 mm counterparts. First results based on data obtained before May 2021 are shown in Bing et al. (2023), which extensively discusses the number counts. At that time, the GOODS-N survey was complete and COSMOS was still missing a factor of 2 in integration time. Since then, the depth of COSMOS has increased, but this flux regime had already been probed by GOODS-N. Therefore, the new data do not significantly improve the constraints on the number counts. For the GOODS-N field, the detailed analysis of individual sources is presented in Berta et al. (2025) and Lagache et al. (2026), while the confusion due to undetected sources is covered in Ponthieu et al. (2026). A similar study was also performed on the serendipitous point-source detections in the NIKA2 large program targeting the Sunyaev-Zeldovich effect in galaxy clusters (LPSZ, Désert et al. in prep.).

In this paper, we present the final N2CLS 2 mm data, interpret their color and redshift distributions, and discuss the consequences for 2 mm surveys. In Sect. 2, we introduce the observed (N2CLS) and simulated data used in the paper. We describe the 2 mm catalog together with the methods used to produce it. In Sect. 3, we discuss the properties of the sources, such as their color and their redshift. We then discuss the relevance of 2 mm single-dish and interferometric photometric surveys in identifying the high-redshift populations of dusty star-forming galaxies in Sect. 4. Finally, we present our conclusions in Sect. 5.

2. Data

2.1. The NIKA2 cosmological legacy survey

The N2CLS is a 300 h guaranteed-time large program of the NIKA2 camera at the 30 m IRAM telescope (192-16, PIs: Lagache, Beelen, and Ponthieu). Thanks to its unprecedented mapping speed for a single-dish mm instrument, NIKA2 allowed us to map two popular fields with unprecedented depth, compared to other mm surveys of the same size in GOODS-N, and a similar depth, but a twice larger area than the Ex-MORA survey in COSMOS (Long et al. 2024). For both fields, the data reduction and map making were performed using the pointing and imaging in continuum (PIIC) data reduction pipeline developed and supported by IRAM (Zylka 2013; Berta & Zylka 2019). The beam FWHM is ∼12 arcsec and ∼18 arcsec at 1.2 mm and 2 mm, respectively.

The GOODS-N field covers 159 arcmin^2 with a 1σ depth of 0.17 mJy/beam and 0.047 mJy/beam at 1.2 mm and 2 mm, respectively. All the data were taken between October 2017 and May 2021. After scan selection (i.e. removing scans with higher noise linked to weather instabilities), the total time on source reached 78.0 h and 72.8 h at 1.2 and 2 mm, respectively. The data reduction is described in Bing et al. (2023). These data are close to the confusion limit (Ponthieu et al. 2026).

In the COSMOS field, we achieve a 1σ sensitivity of 0.3 mJy/beam at 1.2 mm and 0.09 mJy/beam at 2 mm, covering an area of 1130 arcmin^2. The data were taken between October 2017 and January 2023. After the scan selection, the total observing time reached 195 h. Bing et al. (2023) presented the analysis of the data obtained before May 2021 (representing on-source time of 78.7 h at 1.2 mm and and 79 h at 2 mm). We used the same method but with an updated version of PIIC to reduce the full dataset (Carvajal-Bohorquez et al. in prep. for the details).

The absolute calibration uncertainty coming from the planet models used to calibrate the NIKA2 data is 5%. The point-source root-mean-square (RMS) calibration uncertainties are about 6% at 1.2 mm and about 3% at 2 mm (Perotto et al. 2020).

2.2. The GOODS-N catalog

We used the 1.2 mm and 2 mm catalogs produced from NIKA2 and described in Bing et al. (2023). The sources were extracted from match-filtered[2] signal-to-noise (S/N) maps by applying a detection threshold. The source fluxes were then measured via

[1] This paper focuses on wavelengths that are strictly longer than 1 mm.

[2] The original maps were cross-correlated by the beam to maximize the S/N ratio of point sources and optimize their detection.

point spread function (PSF) fitting photometry. End-to-end simulations (see Sect. 2.5) provided estimates of the purity (fraction of real sources in the extracted sample) as a function of this threshold. Bing et al. (2023) used a S/N threshold corresponding to 80% purity (3.0 at 1.2 mm and 2.9 at 2 mm). The biases impacting the photometry, such as flux boosting and filtering effects, were corrected using the median ratio between the intrinsic flux in the simulation and the output flux measured using the simulated map. The simulations were also used to compute the flux uncertainties, which are significantly larger than what we could expect from pure uncorrelated noise.

In this paper, we focused on 2 mm sources, selecting only high-reliability 2 mm sources corresponding to a sample purity of 95% (S/N ≥ 4.2). We obtained a subsample of 25 sources[3] that we then matched with the full 1.2 mm catalog (S/N ≥ 3.0 corresponding to 80% purity) using a matching radius of 6.5 arcsec. Only one object had no 1.2 mm counterpart (N2GN_2_13)[4]. This source is close to the noisy edge of the field. We estimated a 5σ upper limit on its flux based on the flux uncertainties of sources located in areas with a similar depth. The catalog is given in Table B.1.

The counterparts of all these sources were identified using a large set of ancillary data and dedicated NOEMA follow up observations. This counterpart identification and the redshift determination is described in a companion paper (Berta et al. 2025). This procedure also shows that 4 of our 25 sources are multiple (N2GN_1_12, N2GN_1_17, N2GN_1_24, N2GN_1_34).

2.3. The COSMOS catalog

The observing time in the COSMOS field has been more than doubled since the source extraction of Bing et al. (2023). Thus, we produced new 1.2 mm and 2 mm catalogs using the full-depth maps, together with updated end-to-end simulations to estimate the sample purity and correct for the flux boosting and filtering effects. The source extraction and flux measurement were performed following the same approach as in GOODS-N. To estimate the purity, we compared the number of sources between end-to-end simulations and pure-noise maps to derive the fraction of spurious sources at a given S/N (see Carvajal-Bohorquez et al. for a full description of the method). We corrected the raw flux densities and estimated uncertainties using the same approach as in GOODS-N, with only minor changes. We estimate that a purity of 95% is reached for a S/N threshold of 4.6, which we then use to produce our secure 2 mm catalog containing 90 objects. The details will be given in Carvajal-Bohorquez et al. (in prep.).

We used a similar matching procedure as the one described for the GOODS-N field to associate the 2 mm source with their 1.2 mm counterparts. The 1.2 mm catalog used for this procedure was cut off at S/N ≥ 3.9, corresponding to 80% purity. We find a 1.2 mm counterpart for 82 of our 90 sources. Two of the 2 mm sources (N2CO_1_8 and N2CO_1_41) split into two 1.2 mm counterparts each thanks to the sharper beam at shorter wavelength. Two other sources (N2CO_2_29 and N2CO_2_61) are complex blends with a clear 1.2 mm emission near the 2 mm source. However, it is unclear what fraction of the 1.2 mm emission comes from the main 2 mm source. For instance, N2CO_2_61 is detected at 1.2 mm, but it is an intriguing case of a complex blend between the faint 1.2 mm emission associated with the radio source COSMOSVLADP_J095951.93+020542.6 and a brighter 1.2 mm dusty neighbor 8.8 arcsec away (Carvajal-Bohorquez et al., in prep.). The final catalog is provided in Tables B.2 and B.3.

To identify the multi-wavelength counterpart(s) corresponding to each N2CLS source, we first searched for a counterpart in ancillary high-resolution (sub)mm interferometric catalogs, which serve as a proxy for accurate source position (following Berta et al. 2025). We used the following datasets, in decreasing order of priority:

- AS2COSMOS (Simpson et al. 2020), which was given highest priority because of the dedicated follow-ups with ALMA of the bright 850 µm SMGs;
- A^{3}COSMOS (Liu et al. 2019), a (sub)mm ALMA archival survey comprising a prior catalog (S/N ≥ 4.35) and a complementary blind catalog (corresponding to sources detected blindly with S/N ≥ 5.4 and not present in the prior catalog). We used the latest available version of the catalogs[5] (2025/03/12).
- Radio JVLA 3 GHz catalog from Smolčić et al. (2017) if no ALMA counterpart was found.

We visually inspected all our sources to verify the proxy positions and to check for any missing counterparts. During this process, we identified three MeerKAT sources (MIGHTEE – MeerKAT International Gigahertz Tiered Extragalactic Exploration survey; Heywood et al. 2022). After pinpointing the precise location of the N2CLS sources using these high-resolution data, we searched for their short-wavelength counterparts to determine a spectroscopic redshift (when available) or a photometric redshift otherwise. We obtained eight spectroscopic redshifts from Chen et al. (2022), complemented by Mitsuhashi et al. (2021) from the brightest AS2COSMOS sources. We also collected 33 spectroscopic redshifts from the COSMOS spectroscopic redshift compilation by Khostovan et al. (2026), three from Jin et al. (2019), three from Brisbin et al. (2017), two from Daddi et al. (2021), one from Hasinger et al. (2018), one from Casey et al. (2015), one from Ikeda et al. (2026), one from Sillassen et al. (2025), one from Jin et al. (2022), one from Jin et al. (2024), and one from Jin (private communication). We also obtained 26 photometric redshifts from the COSMOS2020 catalog (Weaver et al. 2022), 17 from the COSMOS2025 (COSMOS-Web, Shuntov et al. 2025), three from Liu et al. (2019), one from Miettinen et al. (2017), and one from van der Vlugt et al. (2023). The full procedure will be described in Carvajal-Bohorquez et al. (in prep.).

We identified counterparts for 80 2-mm sources (with ten sources having no proxy detections), of which 18 have multiple counterparts. These 18 multiple sources break into 43 galaxies, including 19 with photometric redshifts and 24 with spectroscopic redshifts. Among the remaining 62 sources with a single counterpart, we have 29, 32, and one galaxies with photometric, spectroscopic, and no redshift, respectively. Finally, 11 galaxies were left without a redshift (one galaxy identified through a proxy but without redshift and ten 2-mm sources without proxy). Compared to GOODS-N, the redshift identification completeness is lower, which limits the interpretation of redshift-dependent statistics.

[3] Berta et al. (2025) reported 26 sources, but N2GN_1_26 has a S/N = 4.18 in the latest version of the catalog and, thus, below our selection threshold.

[4] The name of N2GN_2_20 could suggest that it is also a source detected only at 2 mm, but it has a weak detection at 1.2 mm catalog ($S/N_{1.2\,mm}$ = 3.3) complementing the robust 2 mm detection (S/N_{2mm} = 5.1).

[5] https://sites.google.com/view/a3cosmos

2.4. The SIDES simulations

The simulated IR dusty extragalactic sky (SIDES, Béthermin et al. 2017, 2022) is a semi-empirical realistic simulation of the sky from the mid-IR (MIR) to the mm. It is based on a dark-matter halo catalog from N-body numerical simulations projected into a light cone. The stellar mass of the galaxies hosted by the (sub)halos is derived using the abundance matching technique (see, e.g., Behroozi et al. 2010 or Moster et al. 2013 for a description of the method), which reproduces the observed stellar mass function by construction. The star-forming properties were then drawn following empirical scaling relations that included their scatter, such as the relation between the star formation rate (SFR) and the stellar mass (Schreiber et al. 2015). The galaxy population on this relation was tagged as main sequence and the positive outliers as starbursts.

A spectral energy distribution (SED) template was then attributed to each galaxy, depending on whether it is a main sequence or starbursting object. These templates are based on observations, following the observed evolution of the mean radiation field $\langle U \rangle$ with redshift (Magdis et al. 2012; Béthermin et al. 2015a). The $\langle U \rangle$ parameter is related to the dust temperature (approximately $T_{\rm dust} \propto \langle U \rangle^{\frac{1}{4+\beta}}$, where β is the dust spectral index) and it is drawn by assuming an observationally motivated 0.2 dex scatter around the mean evolution. Finally, the SEDs were integrated into broad-band filters. To properly evaluate the impact of cosmic variance on our observations, we used the new 117 deg^2 version of SIDES introduced in Gkogkou et al. (2023, hereafter SIDES-Uchuu).

SIDES includes the free-free and the synchrotron emission of star-forming galaxies in their SED template, assuming the IR-radio correlation of Sargent et al. (2010) and an equality between synchrotron and free-free emission at 30 GHz. The radio galaxies were not included in SIDES, however, they are discussed in Sect. 3.4.

In Bing et al. (2023), we showed that SIDES reproduces well the number counts at both 1.2 and 2 mm from single-dish and interferometric surveys, if we take resolution effects into account. In this paper, we compare SIDES with measured colors and redshift distributions (see Sect. 3) to further validate it in the mm regime, before using it to discuss the relevance of 2 mm surveys (see Sect. 4).

2.5. End-to-end N2CLS simulation based on SIDES

The source fluxes measured by single-dish mm surveys are affected by a large set of effects such as blending, data filtering, correlated noise, or flux boosting. To simulate only the blending effect, we generated noiseless maps using a Gaussian beam for the sources and we extracted the sources to produce the so-called blob catalog.

To include the other effects, we produced end-to-end (hereafter, E2E) simulations based on SIDES and real N2CLS data. The GOODS-N simulations are described in Bing et al. (2023). For COSMOS, we generated a new simulation for the full dataset (see Carvajal-Bohorquez et al. in prep.) using a similar method. For each detector in the arrays, the incident flux is computed as a function of time using the SIDES simulated map and the real pointing coordinates, which vary with time. The resulting detector timelines are then combined with the real detector timelines after reversing the sign of half of them. These new timelines are used to produce simulated maps using PIIC, in which the true sky signal cancels out while the SIDES signal and the true noise remain. We then run the same source extraction procedure, as described in Sects. 2.2 and 2.3. A similar procedure was applied to each of the 117 SIDES-Uchuu 1-deg^2 tiles. For the purposes of this paper, we matched the simulated 2 mm catalog with the 1.2 mm one, using the same procedure as the one applied to the observational catalogs. The result is hereafter called the E2E catalog.

We checked that the number of robust 2 mm sources per simulated COSMOS field (71 ± 16) is compatible at the 1.2-σ level with the N2CLS (90). Bing et al. (2023) also found marginally higher number counts in their shallower COSMOS data than in GOODS-N and SIDES E2E. A similar result was found by Adscheid et al. (2024) using the A3COSMOS archival survey.

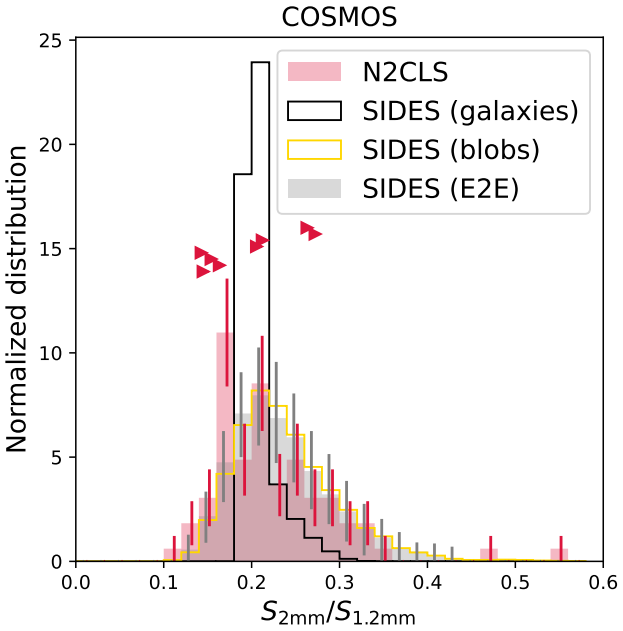

Fig. 1. Distribution of the 2–1.2 mm color for the true N2CLS COSMOS catalog (red filled histogram, only S/N ≥ 4.6 sources at both wavelengths and various simulated catalogs based on SIDES. The solid black histogram corresponds to the simulated SIDES galaxy catalog after applying a flux cut similar to COSMOS data (see Sect. 3.1). The yellow histogram is based on a similar selection, but applied to the blob catalog extracted from the noiseless simulated map. The grey histogram is the distribution obtained using the E2E simulation described in Sect. 2.5. The error bars on the N2CLS histogram are computed assuming a Poisson law, and those from the E2E are the standard deviation between the various simulated fields. The histograms are normalized to have a unity area ($\int n(c)\,dc = 1$, where c is the color). The lower limits on the color of 1.2 mm non-detections are shown as right-pointing triangles. Their y-axis position is arbitrary and was chosen to reduce overcrowding in the figure.

3. Colors and redshifts of the 2 mm sources

3.1. 2 mm versus 1.2 mm colors

Thanks to its simultaneous observations at 1.2 mm and 2 mm, the N2CLS is ideal to study the mm colors of extragalactic sources. We focus our analysis on the COSMOS field for which we have a significantly larger number of detections. Since the color is a ratio, it is affected by the uncertainties on both the numerator and the denominator. Thus, we limited our analysis to high-reliability (S/N ≥ 4.6) sources at both 1.2 mm and 2 mm. However, in COSMOS, this choice has no impact compared to a S/N ≥ 3.9 cut at

Table 1. Comparison of the main characteristics of the 2–1.2 mm color distributions of various catalogs.

Catalog	Mean color	Median color	Standard deviation	KS p-value against N2CLS
N2CLS COSMOS	0.222 ± 0.008	0.206 ± 0.007	0.070 ± 0.010	
SIDES galaxies (COSMOS flux cuts)	0.212 ± 0.003	0.205 ± 0.003	0.022 ± 0.003	2.2×10^{-11}
SIDES blobs (COSMOS flux cuts)	0.240 ± 0.002	0.229 ± 0.002	0.062 ± 0.004	1.9×10^{-3}
SIDES E2E (COSMOS-like)	0.238 ± 0.010	0.227 ± 0.010	0.063 ± 0.012	6.9×10^{-3}

Notes. The N2CLS COSMOS catalog is the true catalog after selecting the high-reliability sources at both 1.2 mm and 2 mm (S/N $\geq$ 4.6). The SIDES galaxy and blob catalogs are both cut at the flux limit of the N2CLS COSMOS field (see Sect. 3.1). The SIDES E2E catalog is described in Sect. 2.5. For the true N2CLS data, the uncertainties on the mean, the median, and the standard deviation are derived using a bootstrap method. For the simulated data, we provide the standard deviation between the multiple COSMOS-like fields extracted from the full SIDES-Uchuu simulation. The impact of the photometric calibration uncertainties on the colors (~7%, see Sect. 3.1) are not taken into account in this table. The last column presents the probability associated with the KS test between a given distribution and the N2CLS.

1.2 mm (80% purity), since there are no robust 2 mm sources with an S/N between 3.9 and 4.6 at 1.2 mm. The measured 2 mm versus 1.2 mm color distribution is shown in Fig. 1. This distribution is asymmetric with a long tail of high color values, corresponding to red objects.

To interpret these data, we computed several distributions based on the SIDES simulation. In this work, we used the 117 deg^2 version of the simulation (Gkogkou et al. 2023) up to $z \sim 7$ to estimate the field-to-field variance. We estimated the impact of this redshift limit using the older 2 deg^2 version with redshifts up to $z = 10$ (Béthermin et al. 2017), and found that it is negligible. For instance, the mean color varies by only 0.3%. For the individual galaxy color distribution, we just cut the SIDES simulated galaxy catalog at the typical flux cut of the N2CLS catalog. For this purpose, we use the S/N limit of 4.6 and multiply it by the mean 1-σ depth of our maps, and obtained the following selection: $S_{2\,mm} \geq 0.414$ mJy and $S_{1.2\,mm} \geq 1.38$ mJy. To evaluate the impact of the NIKA2 angular resolution, we applied similar cuts to the blob catalog presented in Sect. 2.5. Finally, we use the catalogs resulting from our E2E simulations (including real noise in the simulated timelines, the instrumental beam, and map-making effects), which were also introduced in Sect. 2.5 to compare accurately SIDES to N2CLS. Since these simulations produced 117 independent fields with the same field geometry as N2CLS COSMOS, we could use them to estimate the field-to-field variance. These uncertainties are larger than the ones obtained from a bootstrap method, since galaxies in a given region of the sky tend to accumulate at similar redshift and thus have similar colors. These correlations between sources increase the variations between fields of the various summary statistics. The three distributions obtained from SIDES are presented in Fig. 1.

The means and medians of all these distributions are listed in Table 1, and are roughly compatible. The SIDES galaxy catalog have a slightly lower mean but the same median as N2CLS, while the blob and E2E catalogs have higher means and medians. This shows that the resolution effects have a small impact (~10%) on the average colors. To evaluate the quality of SIDES predictions, the most relevant comparison is between the N2CLS and the E2E, since they should be affected by exactly the same instrumental and source extraction effects. The difference between the two means and medians corresponds to 1.2 and 1.7 times the field-to-field standard deviation. We also have to take into account the calibration uncertainties. Because the 1.2 and 2 mm fluxes are affected in the same way (i.e. systematic uncertainty), the absolute calibration uncertainty does not have to be taken into account for the color uncertainty. On the other hand, the point-source rms calibration uncertainties (6% at 1.2 mm and about 3% at 2 mm, Perotto et al. 2020), lead to a 6.7% statistical uncertainty on the color. By quadratically combining these uncertainties with the field-to-field variance, we obtained uncertainties of 0.020 and 0.018 on the mean and the median color, corresponding for both to a 0.8 and 1.1σ difference. Thus, there is no significant tension observed with respect to the average colors of the N2CLS sources and the SIDES predictions.

However, the distributions showed in Fig. 1 exhibit some difference of shapes. The most striking one is how narrow is the SIDES galaxy color distribution compared to the others with a standard deviation which is ~3 times smaller. This is not the case for the SIDES blob catalog, suggesting that the resolution effects drive the dispersion in color rather than the noise. In contrast, the N2CLS and the SIDES E2E catalogs agree on the dispersion at the 0.5σ level, demonstrating how efficiently our E2E simulation can predict the observations.

Despite the agreement between N2CLS and SIDES E2E on these basic metrics, the distributions are not exactly similar. For instance, the probabilities returned by the Kolmogorov-Smirnoff (KS) null-hypothesis test comparing N2CLS and SIDES are always lower than 0.01. Above a p-value of 0.05, we can consider that the two distributions are drawn from the same probability density function. In contrast, a low probability indicates that the two distributions are not similar. This test does not take into account the field-to-field variance and the calibration uncertainties. It may thus be improper and must be interpreted with caution. However, there is a 2.5-σ excess in the 0.16–0.18 bin after taking into account the field-to-field variance. If we exclude this color bin from the KS test, we end up obtaining a p-value of 0.23, confirming that the disagreement is caused by this single bin. The origin of this peak in the color distribution remains unclear.

Finally, we also checked the mean color in the GOODS-N field. This field is limited by its small number of 2 mm detection (25), but it is deeper. We find a mean color of 0.196 ± 0.014, which is compatible with the 0.208 value found in the SIDES galaxy catalog after applying flux cuts similar to GOODS-N ($S_{2\,mm} \geq 0.2$ mJy and $S_{1.2\,mm} \geq 0.71$ mJy. Contrary to COSMOS, we do not observe any excess in the 0.16–0.18 color bin, suggesting this feature is a field variance effect.

3.2. Redshift distribution

The redshift distribution is an important constraint for models. For a flux-limited sample selected at a single wavelength, this distribution varies with both the flux cut and the wavelength (e.g., Smolčić et al. 2012; Zavala et al. 2014; Béthermin et al.

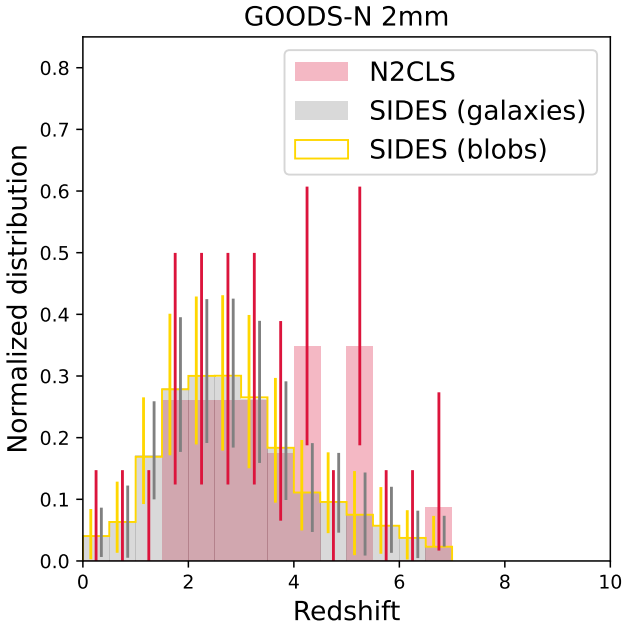

Fig. 2. Redshift distribution of the GOODS-N high-reliability 2 mm sources. The red histogram is the distribution measured in the N2CLS. When sources are multiple, the redshift of the main component is used (see Sect. 3.4). The uncertainties correspond to a Poisson law. The grey histogram is derived from the SIDES galaxy catalog after applying a flux cut similar to the GOODS-N field (see Sect. 3.2). The uncertainties correspond to the field-to-field variance of a $15.9 \times 10\,\mathrm{arcmin}^2$ field. The yellow histogram is based on a similar selection, but applied to the SIDES blob catalog and using the redshift of the brightest galaxy in the beam. The histograms are normalized to have a unity area $\left(\int n(z)\,dz = 1\right)$.

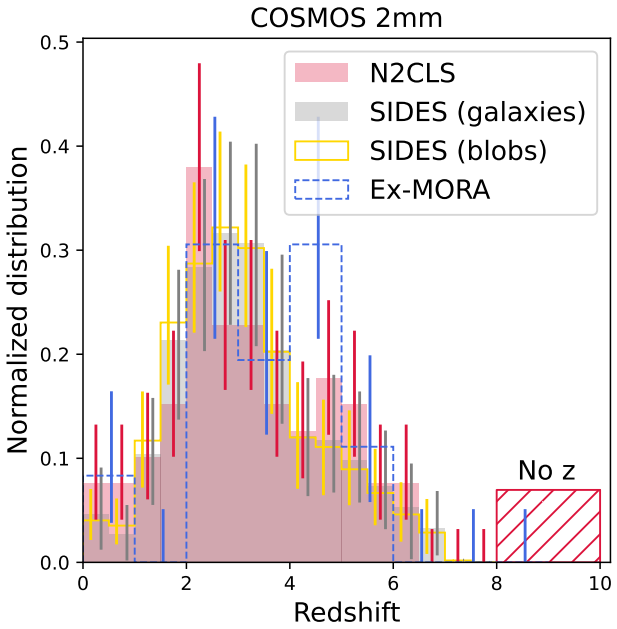

Fig. 3. Same as Fig. 2, but for the COSMOS field. The blue dashed histogram represents the Ex-MORA survey (Long et al. 2024).

2015b). In the (sub)mm, the mean redshift is expected to increase with the wavelength. With its combination of size and depth, the N2CLS 2 mm survey is ideal to test model predictions in the long-wavelength and faint-flux regime. Since it has a complete redshift association, we first focused our analysis on the GOODS-N field where all NIKA2 sources have at least one associated galaxy with a known redshift (Berta et al. 2025).

In Fig. 2, we present the redshift distribution of 2 mm high-reliability sources with Poisson uncertainties. In the case of a multi-component source, we use the redshift of the main component (listed as "a" in Berta et al. 2025)[6]. We compared these results with the predictions from SIDES. The source identification is a complex process involving multi-wavelength data.

Since SIDES does not produce simulated optical and radio images, we had to rely on two simplified approaches. First, we selected a sample in SIDES by cutting the galaxy catalog above the survey flux limit ($S_{2\,mm} \geq S/N_{lim} \times \sigma = 0.2$ mJy). This sharp flux limit is a simplification, since the survey depth varies across the field and the transfer function can also alter the true flux limit. However, the redshift distribution is only weakly dependent on the exact flux cut (Béthermin et al. 2015b), so an approximate flux limit is sufficient for our purpose. Our second approach takes resolution effects into accounts and is based on the SIDES blob catalog. There are always several galaxies with different redshifts present in the same NIKA2 beam, and we attribute the redshift of the brightest galaxy at 2 mm to the blob (see Béthermin et al. 2017, 2024 for a detailed presentation of the method). For both approaches, we compute the field-to-field variance by dividing the SIDES catalog into $15.9 \times 10\,\mathrm{arcmin}^2$ subfields (2541 in total). The galaxy (gray histogram) and blob (yellow histogram) are very similar (see Figs. 2 and 3). This shows that, contrary to the number counts, the redshift distribution is not sensitive to the resolution effects (see, e.g., Bing et al. 2023).

There is an overlap between the 1σ error bars of the N2CLS/GOODS-N and both galaxy and blob SIDES redshift distributions in all the redshift bins except the $5.0 < z < 5.5$ one, where N2CLS is $\sim 1.5\sigma$ above the SIDES predictions. This is due to a known galaxy overdensity at $z \sim 5.2$ around the HDF850.1 galaxy. A companion N2CLS paper shows that this overdensity contain numerous dusty star-forming galaxies (Lagache et al. 2026). There is also an excess in the $4.0 < z < 4.5$ bin, but the 1-σ error bars overlap and, thus, it is not significant. We measure a mean redshift of 3.6 ± 0.3, while the SIDES simulation predicts 2.9 ± 0.2 for both the galaxy and blob selection. The redshift limit at $z \sim 7$ has a minor impact on this quantity and we found a mean redshift of 3.0 using the $2\,\mathrm{deg}^2$ version of SIDES which is cut at $z = 10$ (Béthermin et al. 2017)[7]. This $\sim 2\sigma$ difference is likely due to the overdensity at $z \sim 5.2$.

To test this, we performed a KS test on both redshift distributions after excluding the $5.0 < z < 5.5$ range. The test returns a p-value of 0.4 (same values for the SIDES galaxy and blob catalogs), and N2CLS in GOODS-N and SIDES are thus fully compatible after excluding this known overdensity, while it is only marginally compatible (p-value of 0.06 for both the galaxy and blob catalogs) if we include this redshift bin.

The COSMOS 2 mm catalog is slightly incomplete in redshift (only 88% have a main component with an associated redshift), but has a significantly larger number of detections. We thus performed a similar analysis as in GOODS-N, but using

[6] The source N2GN_1_34 main component has no redshift, and is thus not included in our analysis.

[7] The number of objects as a function of redshift in SIDES exhibit a steady and strong decrease above $z = 4$. The number of $S_{2\,mm} \geq 0.2$ mJy at $z > 7$ is 23, while it is only 3 at $z > 8$ and 0 at $z > 9$. It is thus reasonable to assume that there would be no detectable 2 mm source at $z > 10$ if the simulation was extended to higher redshift.

a $S_{2\,mm}$ flux cut of 0.414 mJy for the SIDES selection and a 34×34 arcmin^2 for the field-to-field variance. This field size matches the 1130 deg^2 area where sources are extracted in the real N2CLS data (Carvajal-Bohorquez et al. in prep.). However, the results should be taken with caution because of the mild redshift incompleteness. The result is shown in Fig. 3. We obtained a mean N2CLS redshift of 3.2 ± 0.2, which agrees with SIDES galaxy prediction of 3.2 ± 0.2 and the blob prediction of 3.1 ± 0.1. The 1σ error bars of the N2CLS COSMOS and the SIDES distribution overlap, and the KS test returns a p-value of 0.58 for the galaxy catalog and 0.47 for the blob catalog, compatible with the two samples being drawn from the same distribution.

We also compared our N2CLS results with those of the ExMORA survey (Long et al. 2024), which has a similar depth and a partial overlap. The redshift distributions of the two surveys agree all the 1-σ error bars overlapping except in the $1< z <2$ bin, where this is almost the case. The KS test p-value is 0.2, confirming the agreement between the two surveys.

Contrary to GOODS-N, there is no tension between the observed and predicted mean redshifts. This suggests that GOODS-N is a peculiar field with a strong overdensity at $z \sim 5.2$. However, COSMOS is slightly incomplete, and could be more incomplete at higher redshift, biasing the mean redshift toward lower values.

3.3. Colors versus redshift

Since the dust emission of galaxies peaks at ~80 µm rest-frame, red colors in the (sub)mm can be used to find high-redshift candidates. For instance, *Herschel* surveys identified sources with red *Herschel*/SPIRE colors (usually 250 versus 500 µm) as $z \gtrsim 4$ candidates (Dowell et al. 2014; Asboth et al. 2016; Donevski et al. 2018). However, Béthermin et al. (2017) and Donevski et al. (2018) showed using simulations that a large fraction of these sources have redder observed colors than their intrinsic ones because of fluctuations of the noise in the bands used to compute the color (positive in the long-wavelength band and negative in the short-wavelength one). Similarly, mm colors were proposed to identify candidates at even higher redshifts (e.g. Casey 2020; Cooper et al. 2022; Cowie et al. 2023). In this section, we study the (sub)mm color of N2CLS galaxies versus redshift to test this approach.

3.3.1. Colors versus redshift in the N2CLS

In the color-versus-redshift relation, we can only place sources which have all their flux coming from the same redshift. Thus, we selected only galaxies with a single counterpart to have no ambiguity. We derived both the N2CLS colors ($S_{2\,mm}/S_{1.2\,mm}$) and the 2 mm versus 850 µm colors after matching our catalogs with the S2COSMOS (Simpson et al. 2017) and SUPER GOODS (Cowie et al. 2017) SCUBA2 catalogs in COSMOS and GOODS-N, respectively. Contrary to Sect. 3.1, we use the full 1.2 mm catalog to compute the colors. The results are presented in Fig. 4.

There is no clear trend of the observed N2CLS $S_{2\,mm}/S_{1.2\,mm}$ color versus redshift (Fig. 4, left) and the data points exhibit a large scatter. For a linear fit of the color versus redshift, we find a slope of 0.009 ± 0.005 when combining GOODS-N and COSMOS. The color measurements are affected by the uncertainties in both the numerator and the denominator. Since we accounted for both the limited S/N and the uncertainties in the deboosting, this can lead to large relative uncertainties (>1/3); thus, the N2CLS sample is too small to detect any significant trend.

The observed evolution of the 2 mm versus 850 µm color with redshift exhibits a tentative mildly increasing trend (Fig. 4, left) with a slope of 0.014 ± 0.006 in COSMOS, corresponding to a 2.3σ significance. This result agrees with Cooper et al. (2022), Cowie et al. (2023), and Long et al. (2024), who also found a weak trend without indicating its significance. We attempted to fit separately the trend below and above $z = 2.5$ (motivated by the trend predicted by SIDES in Sect. 3.3.2). The results are not statistically significant (0.002 ± 0.026 at $z < 2.5$ and 0.017 ± 0.011 at $z > 2.5$), but they are compatible with the flat trend below $z = 2.5$ and the rise above predicted by SIDES.

In the COSMOS field, a small fraction of the sources has no redshift (12%). We compared the color distributions of the sources depending of the type of information on their redshift (see the right side panels of each subfigure of Fig. 4). For the N2CLS $S_{2\,mm}/S_{1.2\,mm}$ colors in COSMOS, the three distributions are similar, except a mild tension between the sources with a spectroscopic redshift and without redshift in COSMOS (p-value of 0.04 to have similar parent distributions according to the KS test). The redshift incompleteness of our sample should thus not affect significantly our results. Concerning the $S_{2\,mm}/S_{850\,\mu m}$ colors in COSMOS, there is a tension between both the photometric and spectroscopic redshift samples and the objects without redshift (p-value of 0.005 and 0.003, respectively). There is no tension between the other distributions. The sources without redshift tend to be redder. It is thus possible that the sample of 11 COSMOS 2 mm galaxies without redshift (no proxy or no redshift available for the counterpart) is biased toward cold or high-z sources.

3.3.2. Colors versus redshift in SIDES

We compared our results with the intrinsic colors of the galaxies in SIDES after applying the same 2 mm flux cut as in Sect. 3.1. We used the 2 deg^2 version of the simulation (Béthermin et al. 2017) for this analysis, since it goes up to $z \sim 10$ and this makes it wide enough for this qualitative comparison. The results are shown in Fig. 4 as grey filled circles. We remark that the intrinsic scatter predicted by SIDES is much smaller than the observational scatter, which is driven by measurement uncertainties. We also computed the mean color of the full SIDES galaxy catalog without applying any flux selection (dashed line). Finally, we derived the evolution of the color in the SIDES blob catalog as a function of the redshift of the brightest component (yellow line and shaded area).

The SIDES simulation includes only a scatter on the mean intensity of the radiation field $\langle U \rangle$, which is directly connected to the dust temperature. In contrast, the slopes of the SEDs in the Rayleigh-Jeans regime have only small variations. Since most of the sources are observed close from this regime, the $S_{2\,mm}/S_{1.2\,mm}$ color at fixed redshift has thus only a very small scatter. We could thus think that SIDES may severely under-predict the color dispersion. However, as shown in Sect. 3.1 and Fig. 1, the observed color scatter is 1-σ compatible with the SIDES scatter after applying all the observational effects. Thus, there is no evidence that the SIDES color scatter is underestimated.

The mean NIKA2 color in both SIDES blob and galaxy catalogs is nearly constant (~0.2) between $z = 0.5$ and 4. It increases slightly at higher redshifts (~0.3 at $z = 8$). The colors obtained for the 2 mm-selected SIDES galaxy (gray symbols) are redder (higher values) than the mean value of all individual galaxies in the SIDES simulation (dashed line). This selection bias will be discussed in Sect. 4.2. The color slightly increases at $z < 0.5$ (as shown by the dashed line for the SIDES mean and the gray

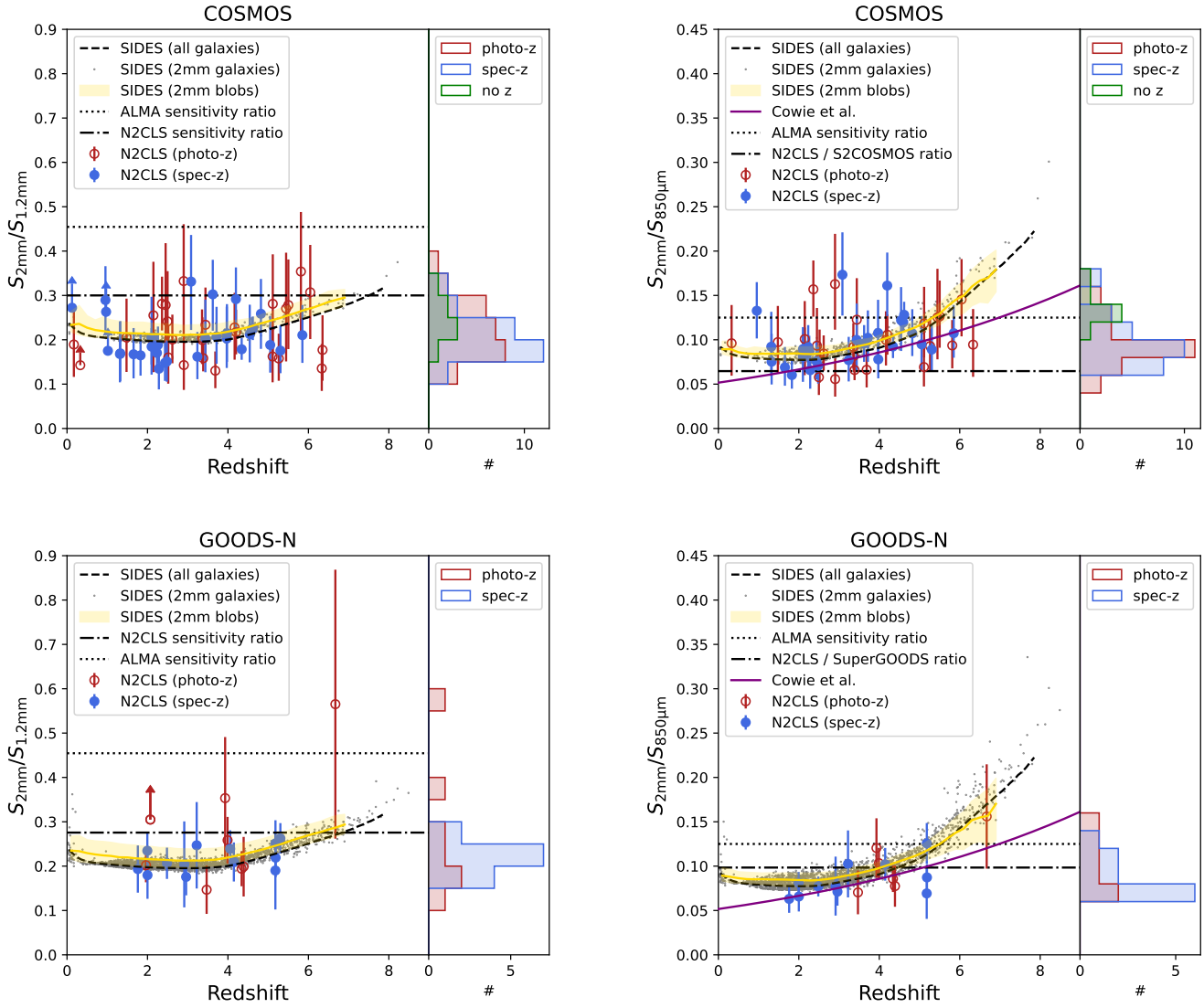

Fig. 4. Color as a function of the redshift in the COSMOS (top) and GOODS-N (bottom) fields. The left plots show the internal NIKA2 color ($S_{2\,mm}/S_{1.2\,mm}$) and the right ones show the ratio between the N2CLS 2 mm and the SCUBA2 850 µm fluxes from S2COSMOS (Simpson et al. 2017) and SUPER GOODS (Cowie et al. 2017). The filled blue circle are the N2CLS sources with spectroscopic redshifts, while the open red circles corresponds to photometric redshifts. The grey dots are from the SIDES 2 deg^2 simulated catalog after applying a 2 mm flux selection similar to SIDES (see Sect. 3.2). The yellow solid line corresponds to the median of the SIDES blob catalog, using the redshift of the brightest galaxy in the beam, and the colored area correspond to the 1σ confidence region. The dashed line is the mean color as a function of redshift from SIDES 2 deg^2 without applying any selection. We also show the sensitivity ratio ($\sigma_{2\,mm}/\sigma_{1.2\,mm}$ where $\sigma_{2\,mm}$ and $\sigma_{1.2\,mm}$ are the RMS of the noise at 2 mm and 1.2 mm, respectively) for ALMA (dotted line) and N2CLS (dot-dashed line). See the discussion in Sect. 4.1 for more details. The right-side panel of each plot show the color distribution of sources with a photometric redshift (red), a spectroscopic redshift (blue), and no redshift (green).

dots for individual 2 mm-selected SIDES galaxies) due to the free-free and synchrotron contributions included in the SIDES templates (Béthermin et al. 2012). Additionally, we note that the blob selection produces slightly redder colors at low redshifts, compared to the 2 mm-selected galaxy catalog.

The results are similar for the $S_{2\,mm}/S_{850\,\mu m}$ color (Fig. 4, right). However, the reddening of the colors with increasing redshift starts at lower redshift ($z \sim 2.5$). This is expected since the Rayleigh-Jeans power-law regime starts above 200 µm rest-frame. Below this rest-frame wavelength, the SED is flatter and this regime is thus reached at lower redshift for the observed 850 µm than the 1.2 mm. The blob catalog produces marginally redder colors at low z and bluer ones at $z > 6$ than the 2 mm-selected galaxy catalog. Cowie et al. (2023) proposed a power-law relation between the logarithm of the color and the redshift ($\log_{10}(S_{2\,mm}/S_{850\,\mu m}) = 0.055z - 1.287$), which disagrees with SIDES forecast at $z < 2$ and $z > 5$. Unfortunately, we lack data in these redshift ranges to test whether SIDES is correct or if the power law is a good approximation.

3.4. 2 mm sources without 1.2 mm counterparts

Because of the expected mild evolution of the NIKA2 color with redshift at $z \gtrsim 4$, the sources detected only at 2 mm could potentially turn out to be at very high redshift. However, our sample has a 95% purity and these sources could thus be spurious.

In the GOODS-N field, only one source (N2GN_2_13) is detected only at 2 mm. As explained in Berta et al. (2025), this

source was detected by NOEMA and has a short-wavelength counterpart with a photometric redshift of 2.071. This suggests that their is no spurious source in the GOODS-N sample. Based on the 25 detections and the 5% spurious rate, we expect in average 1.25 spurious sources per GOODS-N-sized field, and the Poisson probability of having 0 spurious objects in such a field is 0.29. This absence of spurious source is thus compatible with our estimated sample purity.

In the COSMOS field, out of the 90 high-reliability 2 mm sources, we found 8 sources without 1.2 mm counterpart (S/N ≥ 3.9 cut). The two brightest 2 mm-only sources (N2CO_2_37 and N2CO_2_44) are associated (matching distance of 1.40 and 1.42 arcsec, respectively) with two radio sources (COSMOSVLADP_J100114.85+020208.8 and COSMOSVLADP_J095945.19+023439.3, respectively) with spectroscopic redshifts of 0.97 and 0.12, respectively. N2CO_2_37 has a 4 GHz flux density of 7.5 mJy (Schinnerer et al. 2010). Extrapolating this emission at 150 GHz (2 mm) by assuming a standard synchrotron spectrum in $\nu^{-0.8}$, we obtained 0.41 mJy (and 0.59 mJy for $\nu^{-0.7}$). The majority of its 2 mm N2CLS flux (0.71 mJy) is thus expected to come from synchrotron emission. For the second source, which is more than one order of magnitude fainter in radio, the synchrotron is less likely to contribute, but we cannot exclude a contamination of dust emission by some free-free emission.

To understand the nature of the six remaining sources, we used the end-to-end simulation introduced in Sect. 2.5 to estimate the expected number of S/N ≥ 4.6 2 mm sources without S/N ≥ 3.9 1.2 mm counterpart, and found 5.8 ± 3.0 objects. The observations are thus fully compatible with our simulation. We also estimated the probability using another approach by computing the probability to find 6 or more spurious sources assuming a mean expected value of 4.5 (5% spurious rate times 90 sources found in the N2CLS), and found a probability of 0.29. It is thus statistically possible that these 6 sources are all spurious. Searching for these 2 mm-only sources is thus not a reliable way to select very high-z candidates.

3.5. Comparison with the Ex-MORA survey

In the COSMOS field, the extended mapping obscuration to reionization with ALMA (Ex-MORA) survey (Long et al. 2024, see also Casey et al. 2021 and Zavala et al. 2021 for the first MORA survey) has produced an interferometric mosaic of 577 arcmin^2 at 2 mm, overlapping with the N2CLS footprint[8] on 533 arcmin^2. In this section, we compare the Ex-MORA and N2CLS catalogs. The Ex-MORA survey is slightly deeper than N2CLS with flux limit of ∼0.3 mJy versus ∼0.4 mJy. Out of the 37 Ex-MORA sources, four of them are on the noisy edge of the N2CLS field and thus outside of the region where sources were extracted (eMORA.18, eMORA.30, eMORA.31, eMORA.36). Of the 33 remaining Ex-MORA sources, 22 have a corresponding N2CLS 2 mm detection in the full catalog with S/N ≥ 3.9[9] For most of the sources without counterpart, we can observe a faint signal (1.5 ≤ S/N ≤ 3.9) in the N2CLS map at the Ex-MORA position: S/N = 3.4 for eMORA.5, S/N = 3.3 for eMORA.6, S/N = 1.5 for eMORA.9, S/N = 1.9 for eMORA.17, S/N = 2.8 for eMORA.19, S/N = 2.1 for eMORA.23, S/N = 3.6 for eMORA.28, S/N = 2.9 for eMORA.29, S/N = 2.9 for eMORA.32, S/N = 2.5 for eMORA.33. Only the source position of eMORA.34 has no positive fluctuation of the signal (S/N = −0.7), and is among the lowest S/N of the Ex-MORA survey (5.1).

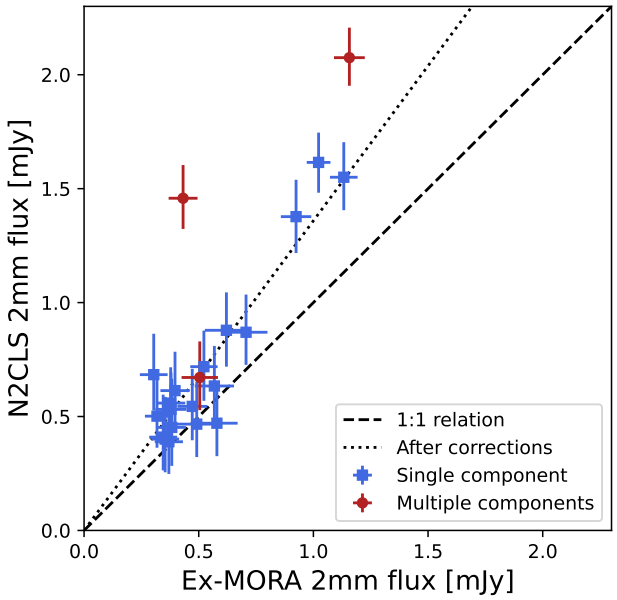

Fig. 5. Comparison between the exMORA (x axis, Long et al. 2024) and N2CLS (y axis) 2 mm flux. The N2CLS sources with a single counterpart are in blue and the multiple sources are in red. The black dashed line indicates the one-to-one relation and the dotted line includes the various corrections (bandpass, source blending, and source sizes) discussed in Sect. 3.5.

We also investigated the Ex-MORA counterparts of robust (S/N ≥ 4.6) N2CLS 2 mm sources. Of the 54 N2CLS sources within the Ex-MORA footprint, only 18 have corresponding Ex-MORA detections within the N2CLS beam (<9 arcsec from the N2CLS centroid). In addition, we inspected the Ex-MORA maps and found at least one candidate source with an S/N > 4 signal in the beam of 13 other N2CLS sources. Four other sources are located in a noisy region at the edge of the Ex-MORA survey, where no detection is possible. Thus, we are left with 19 sources without any significant counterparts in the NIKA2 beam. Only four of them are 2 mm-only detections (see Sect. 3.4) and are potentially spurious. The 15 others are also detected at 1.2 mm and are likely true objects missed by Ex-MORA.

In Fig. 5, we show the comparison between the N2CLS and the Ex-MORA 2 mm flux of objects detected by both surveys. Most of the low-flux source (0.3–0.6 mJy) have compatible fluxes at 2σ, but we can observe a small average excess of N2CLS flux compared to Ex-MORA. This excess is striking at higher flux, where the relative uncertainties are much smaller. A similar excess has been found in GOODS-N for four 2 mm sources followed up by NOEMA (Berta et al. 2025). For sources with a single known component, the N2CLS fluxes have a mean excess ratio of 1.3, and it reaches 2.2 for multiple sources. In the case of multiple sources, the flux difference is straightforward to explain. Indeed, for our multiple sources, Ex-MORA is detecting only one of the counterparts, leading to a significantly smaller Ex-MORA flux than the total flux from the galaxies in the NIKA2 beam.

The origin of the non-unity flux ratio between Ex-MORA and single-component N2CLS sources is less clear. It could be

[8] The overlapping area was computed using MOCPy (Fernique et al. 2022; Baumann et al. 2024). We consider only the region where sources were extracted for the N2CLS.

[9] We used a matching radius of 18 arcsec, but all the counterparts are located at less than 6 arcsec from the Ex-MORA source (1/3 of the beam FWHM) and there is no double matches.

due to the combination of several effects. A first systematic factor comes from the large bandpass of NIKA2 and its different central observed wavelengths compared to Ex-MORA. We compute the flux density ratio between the two instruments assuming a power-law spectrum in $\lambda^{-2.95}$ (or $\nu^{2.95}$) based on the measured mean color between 1.2 mm and 2 mm (Sect. 3.1 and Table 1):

$$\frac{S_{2\,\mathrm{mm}}^{\mathrm{NIKA2}}}{S_{2\,\mathrm{mm}}^{\mathrm{Ex-MORA}}} = \frac{\int \left(\frac{\nu}{\nu_{\mathrm{Ex-MORA}}}\right)^{2.95} t_\nu \, d\nu}{\int t_\nu d\nu} = 1.085, \quad (1)$$

where the central frequency of Ex-MORA is $\nu_{\mathrm{Ex-MORA}} = 147\,\mathrm{GHz}$ and t_ν is the transmission of the NIKA2 2 mm bandpass as a function of frequency. This ratio increase to 1.169 when assuming a modified black body in the Rayleigh-Jeans regime and with an emissivity index β of 2.4, as found by Cooper et al. (2022).

In addition, the flux measured in single-dish blobs can be significantly larger than the flux of the brightest galaxy in the beam (Hayward et al. 2013; Karim et al. 2013; Cowley et al. 2015; Scudder et al. 2016; Béthermin et al. 2017; Bing et al. 2023) due to the presence of other galaxies in the beam. To evaluate the impact of this effect, we compared the flux in the SIDES blob catalog (Sect. 2.5) with the flux of the brightest galaxy in the beam (see Béthermin et al. 2024 for a detailed description of the method), and found a median ratio of 1.14.

Finally, the Ex-MORA flux is measured at the peak of emission, but this method can slightly underestimate the flux if the sources are marginally resolved (e.g., Sect. 3.5 of Béthermin et al. 2020). Assuming Gaussian profiles for both the beam and the galaxy, the peak flux underestimates the total flux by the ratio between the synthesized beam area ($\Omega_{\mathrm{beam}} \propto a_{\mathrm{beam}}\, b_{\mathrm{beam}}$, where a_{beam} and b_{beam} are the beam FWHM of the major and minor axes) and the area of its convolution with the galaxy profile ($\Omega_{\mathrm{beam}} \propto \sqrt{(a_{\mathrm{beam}}^2 + s_{\mathrm{intr}}^2)\,(b_{\mathrm{beam}}^2 + s_{\mathrm{intr}}^2)}$, where s_{intr} is the intrinsic FWHM of the galaxy). For a typical Ex-MORA beam size of 1.68 arcsec × 1.44 arcsec, this leads to an underestimate by a factor of 0.97, 0.91, and 0.71 for a source intrinsic FWHM of 0.25, 0.5, and 1 arcsec, respectively. Thus, this effect is non-negligible even if the galaxies are three times more compact than the beam. The size of the sources can vary from a radius of ∼0.5 kpc to ∼3 kpc (Gómez-Guijarro et al. 2022; Pozzi et al. 2024; Hodge et al. 2025), corresponding to a FWHM from ∼0.1 arcsec to ∼1 arcsec for galaxies between $z = 1$ to $z = 5$. Depending on the source, the effect can range from negligible to strong.

The dotted line in Fig. 5 shows the expected relation between the N2CLS and Ex-MORA flux after applying all these corrections for a source FWHM of 0.5 arcsec and a $\nu^{-2.95}$ reference spectrum. When all these effects are included, there is no longer a discrepancy between the two surveys. The comparison between single-dish and interferometric surveys is thus not straightforward. At similar depth, interferometric surveys will tend to miss extended and multi-component objects, while single-dish surveys will be biased toward groups of galaxies or random alignments. The significant number of N2CLS sources without an Ex-MORA counterpart suggests that these extended and composite sources are not rare. In addition, depending on the exact noise realization in each survey, some sources close to the detection limit may be detected by only one survey. This emphasizes the need for future combined analyses of surveys of the same area at different resolutions.

4. Relevance of 2 mm continuum surveys in searching for high-z DSFGs

The colors and redshifts of the N2CLS 2 mm sources agree with the predictions from the SIDES model (Sects. 3.1, 3.2, and 3.3). In addition, the 2 mm-only sources (only 8 out of 115 N2CLS 2 mm sources for both GOODS-N and COSMOS) are either $z \lesssim 1$ radio sources or are compatible with the expected spurious detection numbers. This tends to rule out the possibility of an exotic population of numerous galaxies detected only at 2 mm at high z or with very cold dust. A similar conclusion is reached by Ponthieu et al. (2026) based the measured N2CLS confusion noise, which is similar to the SIDES predictions. This is also consistent the results of the MORA and Ex-MORA surveys (Casey et al. 2021; Zavala et al. 2021; Long et al. 2024), which also found no excess of exotic very dusty sources. These new data, combined with our model, can also provide insights on the scientific performance (e.g., number of detections, coverage of the SFR-z plane) expected from 2 mm surveys and help us to better understand the impact of the flux selection at this wavelength.

4.1. Based on N2CLS observations

In this section, we discuss the merits of surveys at different wavelengths for detecting galaxies at various redshifts. Here, we consider a wavelength to be more efficient than another if it can detect a source with a higher S/N, or equivalently with less telescope time. Surveys can have different integration times and areas. It is thus important to find a common metric for all of them. In this discussion, we first focus on the case of comparing surveys in different bands (whether simultaneous or not) with the same area Ω_{survey} and total time t_{survey}. Since the sensitivity σ in both bands scales as $t_{\mathrm{survey}}^{-1/2}$ at fixed area and as $\Omega_{\mathrm{survey}}^{-1/2}$ at fixed total time, the sensitivity ratio between the two bands will be invariant as long as the two bands have the same area Ω_{survey} and total time t_{survey}. Sources with a color S_A/S_B equal to the sensitivity ratio σ_A/σ_B will have the same expected S/N in both bands ($S_A/\sigma_A = S_B/\sigma_B$). Sources with colors larger (lower, respectively) than the sensitivity ratio will be detected with a higher S/N in band A (band B, respectively). If most of the sources colors are above (below, respectively) the sensitivity ratio, the survey will be more efficient in band A (band B, respectively).

In Fig. 4, we added the N2CLS sensitivity ratio between 2 mm and 1.2 mm (left panels, dot-dash lines) to enable a comparison with the colors of N2CLS sources. We also computed the sensitivity ratio of ALMA using the observing tool[10]. We estimated the expected sensitivity for 1.5 × 1.5 arcmin^2 continuum mosaic at 150 GHz (2 mm, band 4) and 250 GHz (1.2 mm, band 6) with similar total observing times (5.85 h, 0.02 mJy RMS at 2 mm and 0.044 mJy RMS at 1.2 mm). The chosen size and the total time used in our computation are not important for estimating the sensitivity ratio, if we neglect the discontinuities in the total survey time generated by the need for new calibration cycles when going deeper. In contrast, this method takes into account that more pointings are necessary at higher frequency to cover the same area due to the smaller primary beam. For NIKA2, the 1.2 mm is more efficient than the 2 mm for most of the sources across the full redshift range covered by the N2CLS ($z \lesssim 6.5$). For ALMA, the 1.2 mm is consistently more efficient. A similar comparison can be made between the 2 mm and 850 µm bands. In the case of ALMA, the 850 µm (353 GHz,

[10] https://almascience.eso.org/proposing/observing-tool

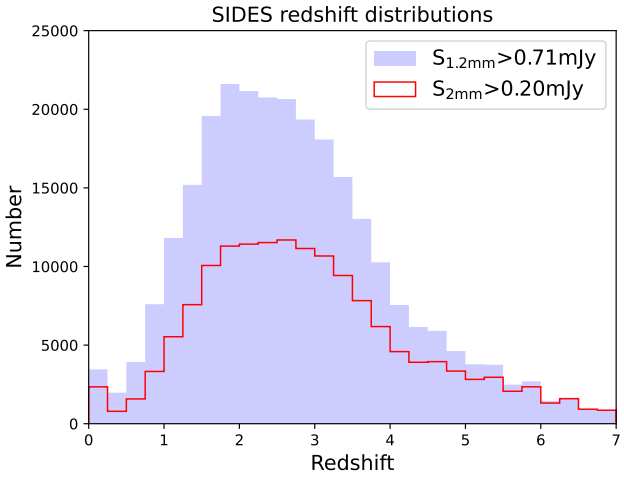

Fig. 6. Redshift distribution of the sources predicted by the 117 deg^2 SIDES simulation for flux cuts at 1.2 mm (blue filled histogram) and 2 mm (red open histogram) similar to N2CLS in GOODS-N.

band; 0.16 mJy RMS on 1.5 × 1.5 arcmin^2 observed in 5.85 h) observations are overall more efficient than those at 2 mm (band 4, 150 GHz). However, the weak trend of the color versus redshift (Sect. 3.3) suggests the possibility of a turnover in favor of the 2 mm band at high redshift. We discuss this possibility based on the SIDES simulation in Sect. 4.2.

The comparison of surveys that use different observational strategies (e.g., total observing time or survey area) and different instruments is less direct. For example, for a fixed total observing time, a narrower and deeper survey may appear more efficient. Therefore, comparisons between different instruments (e.g., SCUBA2 and NIKA2) should be interpreted with caution. N2CLS 2 mm could be considered more efficient than S2CLS 850 µm (Simpson et al. 2017) at all redshifts, although this comes with the caveat that S2CLS covers a larger area. In contrast, SUPER GOODS 850 µm (Cowie et al. 2017) is more efficient than the 2 mm band of the N2CLS at $z \lesssim 4$, but the trend is weak and the turnover redshift is highly uncertain. Overall, 1.2 mm emerges as the most effective wavelength for conducting a census of dusty galaxies in deep blank cosmological surveys.

4.2. Based on SIDES

We can also use the SIDES simulation to estimate the most efficient band across the redshift range. The 2 mm band becomes more efficient than the 1.2 mm band only at $z \gtrsim 7.5$ for NIKA2, and never in the case of ALMA. At these very high redshifts, we do not expect a significant population of heavily dust-obscured sources to be formed (e.g., Michałowski 2015; Burgarella et al. 2020). Concerning the comparison between 2 mm and 850 µm, we confirm that the N2CLS 2 mm band is more efficient than the SUPER GOODS 850 µm data at $z \gtrsim 4$, and than the S2COSMOS 850 µm data at all redshifts. For ALMA, SIDES predicts that the turnover in favor of the 2 mm occurs around $z = 5.5$.

Since SIDES is able to reproduce the current 2 mm observations (see also Bing et al. 2023 for the number counts), we can use this model to better understand the impact of a 2 mm selection. In Fig. 6, we show the predicted redshift distribution of galaxies selected using similar flux limits as N2CLS in GOODS-N (see Sect. 3.2). Contrary to previous observational redshift distributions, these distributions are not normalized, and indicate the total number of detections. This allows us to compare directly the number of expected detections in each redshift bin. The number of sources detected at 2 mm is consistently lower than at 1.2 mm across all bins covered by the simulation ($0 < z < 7$). As expected from the study of the color versus redshift, they start to be similar around $z \sim 7$, where the number of detectable galaxies per redshift interval is a factor of 25 and 13 lower than at the peak around cosmic noon ($z \sim 2.5$) at 1.2 mm and 2 mm, respectively. At cosmic noon, the number of galaxies detected at 2 mm is approximately half of that detected at 1.2 mm.

The higher mean redshift observed in the 2 mm-selected sample is thus primarily due to the reduced number of galaxies detected around cosmic noon, compared to the 1.2 mm selection, rather than an increased sensitivity to higher-redshift sources. Casey et al. (2021) argued that 2-mm surveys are a way to find the needles ($z > 4$ objects) in the haystack (cosmic-noon sources). However, since most of the cosmic noon sources can be identified using ancillary data (Berta et al. 2025), a 1.2 mm selection from which cosmic noon sources are removed is unlikely to produce more higher-z candidates to follow up than a simple 2 mm flux selection. If we use only 2 mm data, we lose information about the dust content of galaxies at cosmic noon (Berta et al. 2025) without adding a significant number of new $z \gtrsim 4$ targets.

Cooper et al. (2022) promoted an alternative approach in which sources are selected at shorter wavelengths (850 µm) from a single-dish survey and then followed up with ALMA at 2 mm to reduce the uncertainties in submm photometric redshifts from $\sigma_z/(1+z) = 0.3$ to $\sigma_z/(1+z) = 0.2$. However, this approach may be less efficient in the JWST era. For most sources, having the location of mm sources with a precision of $\lesssim$1 arcsec is sufficient to find their JWST counterparts and obtain their photometric redshifts. The typical galaxy flux is a factor of ~4 (~10, respectively) times higher at 1.2 mm (850 µm, respectively) than at 2 mm, while ALMA single pointings are only a factor of 1.7 (2.2, respectively) times more sensitive at 2 mm. We can thus follow up ~6 (~20, respectively) times more sources with the same amount of telescope time at 1.2 mm (850 µm, respectively)[11]. Therefore, it may thus be more appropriate to follow up the sources directly at shorter wavelengths (850 µm or 1.2 mm).

Finally, we used SIDES to understand how the selections at various wavelengths are biased toward or against different type of SEDs. The SIDES SEDs are parametrized using the mean radiation field $\langle U \rangle$. High values of this parameter correspond to high dust temperatures. In Fig. 7, we show the redshift evolution of the mean $\langle U \rangle$ parameter together with the 16–84 percentile range corresponding to 1σ in the Gaussian case. In SIDES, the $\langle U \rangle$ distribution varies with redshift but not with the stellar mass. We thus use the full simulated sample including low-mass galaxies[12] to provide our unbiased reference (in grey in the figure). We compare this sample with our flux selections at 1.2 mm (blue) and 2 mm (red) using the N2CLS GOODS-N flux cut. The mean values are biased toward lower $\langle U \rangle$ values (colder dust temperature) by 1σ at $z < 1$ and ~0.5σ at $z \gtrsim 4$. The 2 mm selection is slightly more biased toward high-redshift sources, by approximately 10%. This is not surprising, since colder dust SEDs emit more in the mm at fixed total dust luminosity.

[11] At fixed integration time, the S/N ratio between 1.2 mm and 2 mm is $r = \frac{S_{1.2\,\mathrm{mm}}\sigma_{2\,\mathrm{mm}}}{S_{2\,\mathrm{mm}}\sigma_{1.2\,\mathrm{mm}}}$. Since S/N scales as $\sqrt{t}$, the time necessary to detect a source at a given S/N is thus shorter by a factor r^2 at 1.2 mm.

[12] In SIDES, passive galaxies have a zero flux in both NIKA2 bands and the color is thus not defined. These objects are thus excluded from our analysis.

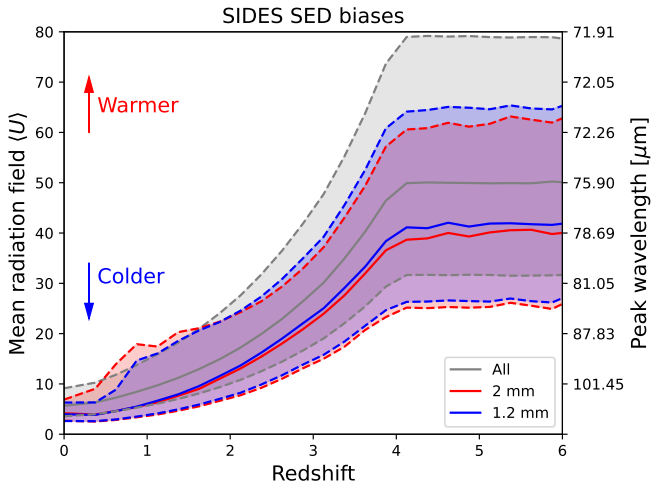

Fig. 7. Mean interstellar radiation field $\langle U \rangle$ as a function of redshift, as predicted by SIDES, illustrating the bias toward colder SEDs introduced by mm flux selections. The mean radiation field is used in SIDES to parametrize the SEDs, and a higher $\langle U \rangle$ corresponds to a higher dust temperature. On the right y-axis, we also indicates the corresponding peak wavelength in S_ν units of the main-sequence SED templates. The solid lines are the mean evolutions as a function of redshift for the full star-forming sample (gray), and selections at 1.2 mm (blue) and 2 mm (red), while the shaded areas and the dashed lines correspond to the 16–84% interval.

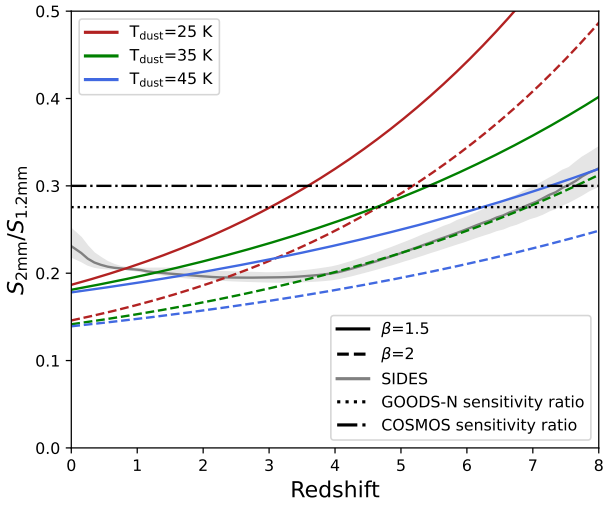

Fig. 8. Relation between the N2CLS color and the redshift for various SED models. The grey solid line and the associated contours represent the median color of SIDES galaxies and the 16–84% dispersion. The solid and dashed colored lines (red for 25 K, green for 35 K, and blue for 45 K) correspond to modified black bodies with $\beta = 1.5$ and $\beta = 2$, respectively. The horizontal lines show the sensitivity ratio in COSMOS (dot-dash line) and GOODS-N (dotted line).

Our modeling analysis is based on the SIDES model, which does not contain a numerous population of dusty galaxies with very cold dust or at very high redshift. In Fig. 8, we show the relation between color and redshift for both SIDES and several modified black body SED models. For SIDES, the 1.2 mm is systematically more sensitive than the 2 mm up to $z \sim 7$. We might consider whether some very cold sources missing in SIDES could be detected at 2 mm, but not at 1.2 mm. To explore this hypothesis, we computed the NIKA2 color expected from modified black bodies ($\nu^\beta B_\nu(T)$) with various dust temperatures T_{dust} and emissivity indices β. Galaxies with $T_{dust} = 25$ K and $\beta = 1.5$ at $z \gtrsim 3.5$ are easier to detect at 2 mm. Galaxies with $T_{dust} = 35$ K and $\beta = 1.5$ or $T_{dust} = 25$ K and $\beta = 2$ are detected first at 2 mm for $z \gtrsim 5$. For other SEDs with a higher T_{dust} or β, the 1.2 mm is more efficient to detect them at least up to $z \sim 7$. If dusty populations at $z \gtrsim 4$ would be mainly objects with very cold dust or a low β, we would have found large populations of galaxies detected at 2 mm or with high $S_{2\,mm}/S_{1.2\,mm}$ colors. Their absence in N2CLS is thus compatible with warmer SEDs, in line with other studies on the evolution the dust temperature with redshift based on small targeted ALMA samples (e.g., Faisst et al. 2020; Sommovigo et al. 2022) or stacking (e.g., Béthermin et al. 2015a; Schreiber et al. 2018; Viero et al. 2022), which found an increasing T_{dust} with redshift.

4.3. Exploring the most efficient approach for mm high-z surveys

The 2 mm surveys as GISMO (Staguhn et al. 2014; Magnelli et al. 2019), N2CLS (Bing et al. 2023; Ponthieu et al. 2026), and (Ex-)MORA (Casey et al. 2021; Long et al. 2024) have opened the 2 mm window for deep and wide high-z galaxy surveys. Unfortunately, these surveys did not reveal any new exotic population. However, they were very important to clarify which dusty sources could be found at $z \gtrsim 4$. With all these data in hands, we can now conclude that the optimal wavelength range to probe the $z \gtrsim 4$ dusty galaxy population is around 1.2 mm, and future surveys should target it in priority. Coverage of the same sky area at 850 μm and 2 mm can help identify some high-redshift candidates; however, this identification remains uncertain due to large color measurement errors caused by limited signal-to-noise, map-making, and source extraction.

Having access to both interferometric and single-dish surveys provides an opportunity to better understand the impact of the angular resolution on the measurements (see Sect. 3.5) and figure out the best observational strategy for future programs. Since high-z dusty sources have a low surface density with $\ll 1$ source per ALMA or NOEMA pointing, probing a large volume could be more efficient using a single-dish mapping and a follow-up of the detections with an interferometer to unambiguously identify their counterparts (e.g., JWST).

We used Ex-MORA and N2CLS as examples to evaluate the merit of a direct interferometric survey against the single-dish approach followed up by interferometric observations. The number of detections per hour is comparable for (Ex-)MORA (37 detections in ∼44 h, combining MORA and Ex-MORA) and N2CLS in COSMOS (90 detections in 195 h). However, the carbon footprint (see Appendix A) and economical cost per hour of observation are dramatically lower for N2CLS at the IRAM 30 m telescope (∼2 /h, private communication, ∼0.1 tCO_2e/h) than (Ex-)MORA at ALMA (∼60 /h, ∼5 tCO_2e/h). The follow up of all robust N2CLS sources in COSMOS would require only 90 ALMA or NOEMA pointings, while (Ex-)MORA is based on 4851 individual ALMA pointings. Thus, these follow-up observations are shorter by several orders of magnitude than a blind interferometric survey. The sum of the cost of a blind single-dish survey and its interferometric follow-up is much lower both on the ecological and economical point of view. This should not be viewed as a shortcoming of (Ex-)MORA, since its final results were published before N2CLS. Rather, this highlights the importance of carefully considering survey strategies when designing future programs. Our discussion applies only to the case of deep surveys. Since a wide range of scientific research can only be conducted with ALMA, efficient use of its observing time is crucial for the scientific community.

In the future, the performance of ALMA will improve (e.g., larger bandpass increasing the continuum sensitivity, potential future multi-beam array). Meanwhile, new generations of single-dish instruments will emerge such as the upgraded version of NIKA2 or TolTEC (Wilson et al. 2020), as well as future single-dish telescopes (e.g., AtLAST, Mroczkowski et al. 2025) will emerge. Therefore, it will be essential to regularly reassess the optimal survey strategy in light of the evolving instrumental landscape and the performance of both interferometric and single-dish facilities.

5. Conclusion

The N2CLS survey produced an unprecedented sample of 115 robust source detections selected at 2 mm (25 in GOODS-N and 90 in COSMOS). This enabled us to constrain their statistical properties, test our models, and gain deeper insights into the types of sources selected by such surveys. Our main results are as follows:

- We measured the mean $S_{2\,mm}/S_{1.2\,mm}$ color of sources detected at both 2 mm and 1.2 mm in the COSMOS field and found 0.222 ± 0.008. Our E2E simulations based on the SIDES model and the N2CLS data themselves show that the full observational process produces biases of ∼10%. We also obtained a scatter of 0.070 ± 0.010 from the observed fluxes. Our simulation shows that the observational process can be responsible for most of this scatter and the intrinsic value could be significantly lower.
- We studied the redshift distribution of the 2 mm sources in both fields. In GOODS-N, we find a mean redshift of 3.6 ± 0.3, which is marginally higher than the prediction from SIDES (2.9 ± 0.2). This high value in GOODS-N is driven by the N2CLS overdensity at $z \sim 5.2$ (Lagache et al. 2026). In the COSMOS field, we found a mean redshift of 3.2 ± 0.2, which is identical to that obtained in SIDES.
- We found that the observed $S_{2\,mm}/S_{1.2\,mm}$ and $S_{2\,mm}/S_{850}$ colors have a large scatter and barely evolves from $z = 0$ to $z = 6$. This suggests that this color cannot be used as a reliable way to select high-z dusty galaxies.
- In COSMOS, there are eight sources detected at 2 mm without counterpart at 1.2 mm. Two of these sources are radio galaxies at $z < 1$. The six other sources are compatible with the expected number of spurious detections. In GOODS-N, only one 2 mm source has no 1.2 mm counterpart, but it is firmly identified as a $z \sim 2$ galaxy thanks to NOEMA follow-up observations.
- We compared the N2CLS 2 mm flux measurements with the Ex-MORA ALMA survey. We observed a NIKA2 flux excess relative to ALMA, not only for sources with multiple components but also for those with a single component, with an average excess factor of 1.3. This is explained by a combination of multiple factors such as the different bandpass of the two surveys, source blending, and peak flux photometry used by Ex-MORA.
- In this paper, we discuss the relevance of 2 mm surveys using both N2CLS and SIDES. We find that the slightly higher mean redshift of 2 mm surveys compared to 1.2 mm is mainly caused by a massive loss of cosmic noon sources, without any significant gain even at $z \gtrsim 5$. The 2 mm sample is also slightly more biased toward colder dust temperatures. Finally, we show that 2 mm single-dish surveys are more efficient than ALMA surveys.

Although the deep 2 mm N2CLS data could presumably have revealed exotic populations of dusty galaxies with very cold dust temperatures or at extremely high redshifts, we found no evidence of such sources. Ruling this out is important for optimizing the wavelength selection of future surveys targeting dusty star-forming galaxies. Our results show that 1.2 mm surveys are more efficient for building large samples from cosmic noon ($z \sim 2$) to the reionization era ($z \sim 8$).

Data availability

The data can be accessed at https://data.lam.fr/n2cls/

Acknowledgements. We thank Arianna Long for providing various Ex-MORA products allowing us to compare our results. We thank Jürgen Knödlseder for providing us the carbon footprint estimates of ALMA and the 30 m telescopes. We acknowledge financial support from the Programme National de Cosmologie and Galaxies (PNCG) funded by CNRS/INSU-IN2P3-INP, CEA and CNES, France, and from the European Research Council (ERC) under the European Union's Horizon 2020 research and innovation programme (project CONCERTO, grant agreement No 788212). This work is based on observations carried out under project numbers 192-16 with the IRAM 30-m telescope, and projects W21CV, W23CX, and S24CF with NOEMA. IRAM is supported by INSU/CNRS (France), MPG (Germany) and IGN (Spain). We would like to thank the IRAM staff for their support during the NIKA and NIKA2 campaigns. The NIKA2 dilution cryostat has been designed and built at the Institut Néel. In particular, we acknowledge the crucial contribution of the Cryogenics Group, and in particular Gregory Garde, Henri Rodenas, Jean Paul Leggeri, Philippe Camus. This work has been partially funded by the Foundation Nanoscience Grenoble and the LabEx FOCUS ANR-11-LABX-0013. This work is supported by the French National Research Agency under the contracts "MKIDS", "NIKA" and ANR-15-CE31-0017 and in the framework of the "Investissements d'avenir" program (ANR-15-IDEX-02). This work has benefited from the support of the European Research Council Advanced Grant ORISTARS under the European Union's Seventh Framework Programme (Grant Agreement no. 291294). F.R. acknowledges financial supports provided by NASA through SAO Award Number SV2-82023 issued by the Chandra X-Ray Observatory Center, which is operated by the Smithsonian Astrophysical Observatory for and on behalf of NASA under contract NAS8-03060. The NIKA2 data were processed using the Pointing and Imaging In Continuum software (PIIC, Zylka 2013; Berta & Zylka 2019), developed by Robert Zylka at the Institut de Radioastronomie Millimetrique (IRAM) and distributed by IRAM via the GILDAS pages. PIIC is the extension of the MOPSIC data reduction software to the case of NIKA2 data. The National Radio Astronomy Observatory is a facility of the National Science Foundation operated under cooperative agreement by Associated Universities, Inc. This work made use of Astropy (http://www.astropy.org): a community-developed core Python package and an ecosystem of tools and resources for astronomy (Astropy Collaboration 2013, 2018, 2022). R.A. was supported by the French government through the France 2030 investment plan managed by the National Research Agency (ANR), as part of the Initiative of Excellence of Université Côte d'Azur under reference number ANR-15-IDEX-01.

References

Adam, R., Adane, A., Ade, P. A. R., et al. 2018, A&A, 609, A115
Adscheid, S., Magnelli, B., Liu, D., et al. 2024, A&A, 685, A1
Asboth, V., Conley, A., Sayers, J., et al. 2016, MNRAS, 462, 1989
Astropy Collaboration (Robitaille, T. P., et al.) 2013, A&A, 558, A33
Astropy Collaboration (Price-Whelan, A. M., et al.) 2018, AJ, 156, 123
Astropy Collaboration (Price-Whelan, A. M., et al.) 2022, ApJ, 935, 167
Barrufet, L., Oesch, P. A., Bouwens, R., et al. 2023, MNRAS, 522, 3926
Baugh, C. M., Lacey, C. G., Frenk, C. S., et al. 2005, MNRAS, 356, 1191
Baumann, M., Marchand, M., Pineau, F.-X., et al. 2024, https://doi.org/10.5281/zenodo.14205461
Behroozi, P. S., Conroy, C., & Wechsler, R. H. 2010, ApJ, 717, 379
Berta, S., & Zylka, R. 2019, Welcome to the PIIC, https://www.iram.fr/~gildas/dist/piic.pdf
Berta, S., Lagache, G., Beelen, A., et al. 2025, A&A, 696, A193
Béthermin, M., Daddi, E., Magdis, G., et al. 2012, ApJ, 757, L23
Béthermin, M., Daddi, E., Magdis, G., et al. 2015a, A&A, 573, A113
Béthermin, M., De Breuck, C., Sargent, M., & Daddi, E. 2015b, A&A, 576, L9
Béthermin, M., Wu, H.-Y., Lagache, G., et al. 2017, A&A, 607, A89
Béthermin, M., Fudamoto, Y., Ginolfi, M., et al. 2020, A&A, 643, A2
Béthermin, M., Gkogkou, A., Van Cuyck, M., et al. 2022, A&A, 667, A156
Béthermin, M., Bolatto, A. D., Boulanger, F., et al. 2024, A&A, 692, A52
Bing, L., Béthermin, M., Lagache, G., et al. 2023, A&A, 677, A66
Bing, L. J., Beelen, A., Lagache, G., et al. 2024, A&A, 683, A232
Blain, A. W., Smail, I., Ivison, R. J., Kneib, J.-P., & Frayer, D. T. 2002, Phys. Rep., 369, 111

Bourrion, O., Benoit, A., Bouly, J. L., et al. 2016, J. Instrum., 11, P11001
Brisbin, D., Miettinen, O., Aravena, M., et al. 2017, A&A, 608, A15
Burgarella, D., Nanni, A., Hirashita, H., et al. 2020, A&A, 637, A32
Calvo, M., Benoît, A., Catalano, A., et al. 2016, J. Low Temp. Phys., 184, 816
Casey, C. M. 2020, ApJ, 900, 68
Casey, C. M., Narayanan, D., & Cooray, A. 2014, Phys. Rep., 541, 45
Casey, C. M., Cooray, A., Capak, P., et al. 2015, ApJ, 808, L33
Casey, C. M., Zavala, J. A., Aravena, M., et al. 2019, ApJ, 887, 55
Casey, C. M., Zavala, J. A., Manning, S. M., et al. 2021, ApJ, 923, 215
Chapman, S. C., Blain, A. W., Ivison, R. J., & Smail, I. R. 2003, Nature, 422, 695
Chen, C.-C., Liao, C.-L., Smail, I., et al. 2022, ApJ, 929, 159
Cooper, O. R., Casey, C. M., Zavala, J. A., et al. 2022, ApJ, 930, 32
Cowie, L. L., Barger, A. J., Hsu, L. Y., et al. 2017, ApJ, 837, 139
Cowie, L. L., Barger, A. J., & Bauer, F. E. 2023, ApJ, 952, 28
Cowley, W. I., Lacey, C. G., Baugh, C. M., & Cole, S. 2015, MNRAS, 446, 1784
Daddi, E., Valentino, F., Rich, R. M., et al. 2021, A&A, 649, A78
Donevski, D., Buat, V., Boone, F., et al. 2018, A&A, 614, A33
Dowell, C. D., Conley, A., Glenn, J., et al. 2014, ApJ, 780, 75
Dunlop, J. S., McLure, R. J., Biggs, A. D., et al. 2017, MNRAS, 466, 861
Faisst, A. L., Fudamoto, Y., Oesch, P. A., et al. 2020, MNRAS, 498, 4192
Fernique, P., Nebot, A., Durand, D., et al. 2022, MOC: Multi-Order Coverage map Version 2.0, IVOA Recommendation 27 July 2022
Franco, M., Elbaz, D., Béthermin, M., et al. 2018, A&A, 620, A152
Fudamoto, Y., Oesch, P. A., Schouws, S., et al. 2021, Nature, 597, 489
Gkogkou, A., Béthermin, M., Lagache, G., et al. 2023, A&A, 670, A16
Gómez-Guijarro, C., Elbaz, D., Xiao, M., et al. 2022, A&A, 658, A43
Gruppioni, C., Béthermin, M., Loiacono, F., et al. 2020, A&A, 643, A8
Hasinger, G., Capak, P., Salvato, M., et al. 2018, ApJ, 858, 77
Hayward, C. C., Behroozi, P. S., Somerville, R. S., et al. 2013, MNRAS, 434, 2572
Hayward, C. C., Sparre, M., Chapman, S. C., et al. 2021, MNRAS, 502, 2922
Heywood, I., Jarvis, M. J., Hale, C. L., et al. 2022, MNRAS, 509, 2150
Hodge, J. A., & da Cunha, E. 2020, R. Soc. Open Sci., 7, 200556
Hodge, J. A., da Cunha, E., Kendrew, S., et al. 2025, ApJ, 978, 165
Holland, W. S., Robson, E. I., Gear, W. K., et al. 1999, MNRAS, 303, 659
Hughes, D. H., Serjeant, S., Dunlop, J., et al. 1998, Nature, 394, 241
Ikeda, R., Iono, D., Tadaki, K.-I., et al. 2026, ApJ, 996, 121
Jin, S., Daddi, E., Magdis, G. E., et al. 2019, ApJ, 887, 144
Jin, S., Daddi, E., Magdis, G. E., et al. 2022, A&A, 665, A3
Jin, S., Sillassen, N. B., Hodge, J., et al. 2024, A&A, 690, L16
Karim, A., Swinbank, A. M., Hodge, J. A., et al. 2013, MNRAS, 432, 2
Khostovan, A. A., Kartaltepe, J. S., Salvato, M., et al. 2026, ApJS, 282, 6
Khusanova, Y., Bethermin, M., Le Fèvre, O., et al. 2021, A&A, 649, A152
Knödlseder, J., Coriat, M., Garnier, P., & Hughes, A. 2024, Nat. Astron., 8, 1478
Kumar, A., Artale, M. C., Montero-Dorta, A. D., et al. 2025, A&A, 698, A236
Lagache, G., Dole, H., Puget, J.-L., et al. 2004, ApJS, 154, 112
Lagache, G., Xiao, M., Beelen, A., et al. 2026, A&A, 705, A214
Laurent, G. T., Aguirre, J. E., Glenn, J., et al. 2005, ApJ, 623, 742
Lestrade, J. F., Combes, F., Salomé, P., et al. 2010, A&A, 522, L4
Lindner, R. R., Baker, A. J., Omont, A., et al. 2011, ApJ, 737, 83
Liu, D., Lang, P., Magnelli, B., et al. 2019, ApJS, 244, 40
Long, A. S., Casey, C. M., McKinney, J., et al. 2024, ApJ, submitted [arXiv:2408.14546]
Lovell, C. C., Geach, J. E., Davé, R., Narayanan, D., & Li, Q. 2021, MNRAS, 502, 772
Magdis, G. E., Daddi, E., Béthermin, M., et al. 2012, ApJ, 760, 6
Magnelli, B., Karim, A., Staguhn, J., et al. 2019, ApJ, 877, 45
Michałowski, M. J. 2015, A&A, 577, A80
Miettinen, O., Delvecchio, I., Smolčić, V., et al. 2017, A&A, 606, A17
Mitsuhashi, I., Matsuda, Y., Smail, I., et al. 2021, ApJ, 907, 122
Monfardini, A., Adam, R., Adane, A., et al. 2014, J. Low Temp. Phys., 176, 787
Moster, B. P., Naab, T., & White, S. D. M. 2013, MNRAS, 428, 3121
Mroczkowski, T., Gallardo, P. A., Timpe, M., et al. 2025, A&A, 694, A142
Perotto, L., Ponthieu, N., Macías-Pérez, J. F., et al. 2020, A&A, 637, A71
Ponthieu, N., Désert, F.-X., Beelen, A., et al. 2026, A&A, 705, A213
Pozzi, F., Calura, F., D'Amato, Q., et al. 2024, A&A, 686, A187
Sargent, M. T., Schinnerer, E., Murphy, E., et al. 2010, ApJ, 714, L190
Schinnerer, E., Sargent, M. T., Bondi, M., et al. 2010, ApJS, 188, 384
Schreiber, C., Pannella, M., Elbaz, D., et al. 2015, A&A, 575, A74
Schreiber, C., Elbaz, D., Pannella, M., et al. 2018, A&A, 609, A30
Scott, K. S., Wilson, G. W., Aretxaga, I., et al. 2012, MNRAS, 423, 575
Scudder, J. M., Oliver, S., Hurley, P. D., et al. 2016, MNRAS, 460, 1119
Shuntov, M., Akins, H. B., Paquereau, L., et al. 2025, A&A, 704, A339
Sillassen, N. B., Jin, S., Magdis, G. E., et al. 2025, A&A, 693, A309
Simpson, J. M., Swinbank, A. M., Smail, I., et al. 2014, ApJ, 788, 125
Simpson, J. M., Smail, I., Swinbank, A. M., et al. 2017, ApJ, 839, 58
Simpson, J. M., Smail, I., Dudzevičiūtė, U., et al. 2020, MNRAS, 495, 3409
Smail, I., Ivison, R. J., & Blain, A. W. 1997, ApJ, 490, L5
Smolčić, V., Aravena, M., Navarrete, F., et al. 2012, A&A, 548, A4
Smolčić, V., Novak, M., Bondi, M., et al. 2017, A&A, 602, A1
Sommovigo, L., Ferrara, A., Pallottini, A., et al. 2022, MNRAS, 513, 3122
Staguhn, J. G., Kovács, A., Arendt, R. G., et al. 2014, ApJ, 790, 77
Strandet, M. L., Weiss, A., De Breuck, C., et al. 2017, ApJ, 842, L15
Talia, M., Cimatti, A., Giulietti, M., et al. 2021, ApJ, 909, 23
van der Vlugt, D., Hodge, J. A., Jin, S., et al. 2023, ApJ, 951, 131
Vieira, J. D., Marrone, D. P., Chapman, S. C., et al. 2013, Nature, 495, 344
Viero, M. P., Sun, G., Chung, D. T., Moncelsi, L., & Condon, S. S. 2022, MNRAS, 516, L30
Wang, T., Schreiber, C., Elbaz, D., et al. 2019, Nature, 572, 211
Weaver, J. R., Kauffmann, O. B., Ilbert, O., et al. 2022, ApJS, 258, 11
Weiß, A., De Breuck, C., Marrone, D. P., et al. 2013, ApJ, 767, 88
Wilson, G. W., Abi-Saad, S., Ade, P., et al. 2020, SPIE Conf. Ser., 11453, 1145302
Zavala, J. A., Aretxaga, I., & Hughes, D. H. 2014, MNRAS, 443, 2384
Zavala, J. A., Casey, C. M., Manning, S. M., et al. 2021, ApJ, 909, 165
Zylka, R. 2013, Astrophysics Source Code Library [record ascl:1303.011]

[1] Université de Strasbourg, CNRS, Observatoire astronomique de Strasbourg, UMR 7550, 67000 Strasbourg, France
[2] Aix Marseille Univ, CNRS, CNES, LAM (Laboratoire d'Astrophysique de Marseille), Marseille, France
[3] Université Côte d'Azur, Observatoire de la Côte d'Azur, CNRS, Laboratoire Lagrange, France
[4] School of Physics and Astronomy, Cardiff University, Queen's Buildings, The Parade, Cardiff CF24 3AA, UK
[5] Université Paris Cité, Université Paris-Saclay, CEA, CNRS, AIM, F-91191 Gif-sur-Yvette, France
[6] Institut de Radioastronomie Millimétrique (IRAM), Avenida Divina Pastora 7, Local 20, E-18012 Granada, Spain
[7] Institut Néel, CNRS, Université Grenoble Alpes, Grenoble, France
[8] Astronomy Centre, Department of Physics and Astronomy, University of Sussex, Brighton BN1 9QH, United Kingdom
[9] Institut de RadioAstronomie Millimétrique (IRAM), Grenoble, France
[10] Univ. Grenoble Alpes, CNRS, Grenoble INP, LPSC-IN2P3, 53, avenue des Martyrs, 38000 Grenoble, France
[11] Dipartimento di Fisica, Sapienza Università di Roma, Piazzale Aldo Moro 5, I-00185 Roma, Italy
[12] Univ. Grenoble Alpes, CNRS, IPAG, 38000 Grenoble, France
[13] Institute for Research in Fundamental Sciences (IPM), School of Astronomy, Tehran, Iran
[14] Centro de Astrobiología (CSIC-INTA), Torrejón de Ardoz, 28850 Madrid, Spain
[15] Aix Marseille Univ, CNRS/IN2P3, CPPM, Marseille, France
[16] National Observatory of Athens, Institute for Astronomy, Astrophysics, Space Applications and Remote Sensing, Ioannou Metaxa and Vasileos Pavlou, GR-15236 Athens, Greece
[17] Department of Astrophysics, Astronomy & Mechanics, Faculty of Physics, University of Athens, Panepistimiopolis, GR-15784 Zografos, Athens, Greece
[18] High Energy Physics Division, Argonne National Laboratory, 9700 South Cass Avenue, Lemont, IL 60439, USA
[19] LERMA, Observatoire de Paris, PSL Research University, CNRS, Sorbonne Université, UPMC, 75014 Paris, France
[20] Institute of Space Sciences (ICE), CSIC, Campus UAB, Carrer de Can Magrans s/n, E-08193 Barcelona, Spain
[21] ICREA, Pg. Lluís Companys 23, Barcelona, Spain
[22] IRAP, CNRS, Université de Toulouse, CNES, UT3-UPS, (Toulouse), France
[23] Dipartimento di Fisica, Università di Roma 'Tor Vergata', Via della Ricerca Scientifica 1, I-00133 Roma, Italy
[24] School of Physics and Astronomy, University of Leeds, Leeds LS2 9JT, UK
[25] Institut d'Astrophysique de Paris, CNRS (UMR7095), 98 bis boulevard Arago, 75014 Paris, France
[26] University of Lyon, UCB Lyon 1, CNRS/IN2P3, IP2I, 69622 Villeurbanne, France

Table B.1. High-quality (95 % purity) 2 mm N2CLS catalog in the GOODS-N field.

N2CLS name	IAU name	R.A.$_{2\,mm}$ deg	Dec$_{2\,mm}$ deg	S/N$_{2\,mm}$	S$_{2\,mm}$ mJy	S/N$_{1.2\,mm}$	S$_{1.2\,mm}$ mJy
N2GN_1_01	N2GN J123633+621408	189.1400	62.2361	35.7	$1.22^{0.13}_{-0.12}$	40.0	$5.00^{0.48}_{-0.48}$
N2GN_1_02	N2GN J123730+621259	189.3786	62.2160	16.6	$0.86^{0.15}_{-0.13}$	25.6	$4.77^{0.43}_{-0.58}$
N2GN_1_03	N2GN J123707+621408	189.2802	62.2355	15.3	$0.52^{0.07}_{-0.09}$	23.2	$2.91^{0.30}_{-0.22}$
N2GN_1_04	N2GN J123711+622211	189.2991	62.3700	18.8	$1.85^{0.29}_{-0.23}$	21.4	$8.06^{0.68}_{-0.91}$
N2GN_1_05	N2GN J123711+621330	189.2988	62.2253	16.0	$0.60^{0.10}_{-0.08}$	20.6	$2.71^{0.28}_{-0.31}$
N2GN_1_06	N2GN J123652+621226	189.2160	62.2072	13.3	$0.46^{0.09}_{-0.08}$	19.1	$2.36^{0.23}_{-0.29}$
N2GN_1_07	N2GN J123645+621448	189.1923	62.2470	9.3	$0.31^{0.06}_{-0.09}$	19.0	$2.29^{0.24}_{-0.22}$
N2GN_1_08	N2GN J123631+621714	189.1333	62.2875	11.3	$0.56^{0.12}_{-0.11}$	18.0	$3.38^{0.42}_{-0.43}$
N2GN_1_09	N2GN J123627+621217	189.1139	62.2046	10.6	$0.36^{0.08}_{-0.08}$	18.0	$2.20^{0.31}_{-0.25}$
N2GN_1_11	N2GN J123713+621826	189.3081	62.3072	13.1	$0.49^{0.08}_{-0.09}$	15.2	$2.14^{0.33}_{-0.29}$
N2GN_1_12	N2GN J123636+621155	189.1530	62.1985	8.3	$0.27^{0.10}_{-0.07}$	15.1	$1.79^{0.25}_{-0.29}$
N2GN_1_13	N2GN J123658+621451	189.2440	62.2476	11.7	$0.37^{0.07}_{-0.08}$	14.6	$1.71^{0.21}_{-0.25}$
N2GN_1_14	N2GN J123701+621146	189.2567	62.1963	6.7	$0.28^{0.10}_{-0.09}$	13.3	$1.88^{0.25}_{-0.27}$
N2GN_1_15	N2GN J123618+621550	189.0762	62.2640	6.6	$0.32^{0.10}_{-0.12}$	13.2	$2.38^{0.43}_{-0.35}$
N2GN_1_16	N2GN J123622+621615	189.0930	62.2721	4.7	$0.23^{0.13}_{-0.12}$	12.5	$2.33^{0.37}_{-0.35}$
N2GN_1_17	N2GN J123738+621734	189.4097	62.2934	11.4	$0.51^{0.10}_{-0.11}$	11.9	$2.00^{0.31}_{-0.42}$
N2GN_1_18	N2GN J123702+621425	189.2619	62.2413	6.7	$0.21^{0.08}_{-0.09}$	11.6	$1.36^{0.27}_{-0.21}$
N2GN_1_23	N2GN J123656+621207	189.2333	62.2023	4.7	$0.17^{0.11}_{-0.09}$	9.5	$1.23^{0.31}_{-0.29}$
N2GN_1_24	N2GN J123719+621219	189.3289	62.2048	4.2	$0.20^{0.18}_{-0.12}$	8.9	$1.49^{0.34}_{-0.37}$
N2GN_1_25	N2GN J123712+621212	189.3037	62.2026	4.6	$0.20^{0.13}_{-0.11}$	8.7	$1.32^{0.34}_{-0.26}$
N2GN_1_28	N2GN J123728+621920	189.3638	62.3227	5.8	$0.27^{0.13}_{-0.13}$	7.9	$1.38^{0.39}_{-0.36}$
N2GN_1_34	N2GN J123644+621938	189.1864	62.3275	5.6	$0.36^{0.19}_{-0.14}$	6.9	$1.63^{0.61}_{-0.50}$
N2GN_1_36	N2GN J123658+620930	189.2443	62.1585	6.4	$0.36^{0.14}_{-0.14}$	6.0	$1.19^{0.43}_{-0.38}$
N2GN_2_13	N2GN J123720+621128	189.3374	62.1913	7.4	$0.43^{0.11}_{-0.14}$	–	<2
N2GN_2_20	N2GN J123608+621251	189.0370	62.2142	5.1	$0.24^{0.13}_{-0.12}$	3.3	$0.52^{0.29}_{-0.28}$

Notes. The first and second columns: N2CLS short names and the IAU names, respectively. The R.A.$_{2\,mm}$ and Dec$_{2\,mm}$ columns are the coordinates of the sources measured in the 2 mm maps. The four last columns (S/N$_{2\,mm}$, S$_{2\,mm}$, S/N$_{1.2\,mm}$ et S$_{1.2\,mm}$) are the S/N at 2 mm, the N2CLS flux at 2 mm, the S/N at 1.2 mm, and the N2CLS flux at 1.2 mm, respectively. For the source without 1.2 mm counterpart, we provide a 5 σ upper limit on the flux. The redshifts are provided in Berta et al. (2025).

Appendix A: Estimate of the carbon footprint of ALMA and the IRAM 30 m telescope

Knödlseder et al. (2024) estimated the carbon footprint of worldwide astronomical research facilities. They provided us their best estimate of the yearly carbon footprint of ALMA and the IRAM 30 m telescope on which the NIKA2 camera is installed. For ALMA, they estimated 256 000 tCO_2e for the construction and 21 000 tCO_2e/yr for the operations. For the 30 m, the construction produced 4700 tCO_2e and the operations 300 tCO_2e. If we distribute the construction impact over an assumed 50 yr of operation, we obtain 26 000 tCO_2e/yr for ALMA and 400 tCO_2e/yr. for the 30 m. Thus, there is a ratio of 65 between the two carbon footprints. Both observatories declare ~4000-5000 h of useful science data per year, although the 30 m tends to observe at lower frequency. Even when trying to correct for the better weather at ALMA for 2 mm observations, it is rather safe to assume that the hourly carbon footprint ratio between the two facilites is at least 1.5 orders of magnitude higher.

Appendix B: Tables

The N2CLS robust (95 % purity) 2 mm catalogs are presented in Table B.1 for GOODS-N and Table B.2 and B.3 for COSMOS. All the data used in this paper (1.2 and 2 mm fluxes from N2CLS, 850 μm fluxes from SCUBA2, redshifts, and simulations) can be accessed at https://data.lam.fr/n2cls/.

Table B.2. High-quality (95 % purity) 2 mm N2CLS catalog in the GOODS-N field.

N2CLS name	IAU name	R.A.$_{2\,mm}$ deg	Dec$_{2\,mm}$ deg	S/N$_{2\,mm}$	S$_{2\,mm}$ mJy	S/N$_{1.2\,mm}$	S$_{1.2\,mm}$ mJy
N2CO_1_1	N2CO J100008+022612	150.0332	2.4369	22.0	$2.07^{0.13}_{-0.12}$	28.1	$9.20^{0.52}_{-0.64}$
N2CO_1_2	N2CO J100015+021549	150.0647	2.2638	17.1	$1.62^{0.13}_{-0.13}$	22.6	$7.18^{0.48}_{-0.58}$
N2CO_1_3	N2CO J095942+022937	149.9283	2.4940	14.3	$1.38^{0.16}_{-0.16}$	22.4	$7.71^{0.50}_{-0.62}$
N2CO_1_4	N2CO J100057+022014	150.2379	2.3372	16.0	$1.46^{0.15}_{-0.13}$	21.8	$6.84^{0.46}_{-0.45}$
N2CO_1_5	N2CO J095957+022731	149.9886	2.4588	16.1	$1.55^{0.15}_{-0.14}$	20.4	$6.87^{0.48}_{-0.44}$
N2CO_1_6	N2CO J100122+022005	150.3459	2.3346	11.9	$1.49^{0.22}_{-0.20}$	17.7	$7.18^{0.63}_{-0.65}$
N2CO_1_7	N2CO J100019+023204	150.0818	2.5349	9.4	$0.87^{0.17}_{-0.14}$	17.0	$5.49^{0.49}_{-0.49}$
N2CO_1_8[a]	N2CO J095959+023442	149.9966	2.5797	12.0	$1.42^{0.21}_{-0.20}$	15.2	$10.24^{0.88}_{-0.86}$
N2CO_1_9	N2CO J100028+023204	150.1195	2.5347	9.2	$0.88^{0.17}_{-0.16}$	14.2	$4.66^{0.54}_{-0.52}$
N2CO_1_10	N2CO J100031+021241	150.1326	2.2115	8.7	$0.81^{0.16}_{-0.15}$	14.0	$4.36^{0.52}_{-0.50}$
N2CO_1_11	N2CO J100043+020519	150.1797	2.0890	5.3	$0.50^{0.16}_{-0.14}$	13.7	$4.39^{0.53}_{-0.49}$
N2CO_1_12	N2CO J100121+023129	150.3404	2.5253	5.6	$0.68^{0.21}_{-0.19}$	12.9	$5.23^{0.63}_{-0.61}$
N2CO_1_13	N2CO J100034+020302	150.1429	2.0509	6.4	$0.61^{0.17}_{-0.15}$	12.7	$4.10^{0.51}_{-0.50}$
N2CO_1_14	N2CO J095959+020633	149.9995	2.1096	7.2	$0.67^{0.16}_{-0.14}$	12.6	$3.93^{0.50}_{-0.46}$
N2CO_1_16	N2CO J100025+022606	150.1048	2.4345	7.4	$0.70^{0.16}_{-0.15}$	12.3	$3.93^{0.52}_{-0.51}$
N2CO_1_17	N2CO J100023+021750	150.1004	2.2977	7.3	$0.69^{0.16}_{-0.15}$	12.2	$3.94^{0.52}_{-0.51}$
N2CO_1_18	N2CO J100033+022600	150.1386	2.4335	7.2	$0.67^{0.16}_{-0.14}$	11.9	$3.88^{0.53}_{-0.51}$
N2CO_1_19	N2CO J100004+023046	150.0205	2.5127	6.0	$0.56^{0.16}_{-0.15}$	11.6	$3.70^{0.50}_{-0.48}$
N2CO_1_20	N2CO J100010+021335	150.0419	2.2266	7.8	$0.72^{0.16}_{-0.15}$	11.5	$3.61^{0.49}_{-0.48}$
N2CO_1_21	N2CO J100033+020850	150.1405	2.1474	8.8	$0.83^{0.16}_{-0.16}$	11.5	$3.84^{0.52}_{-0.50}$
N2CO_1_22	N2CO J100038+020823	150.1584	2.1394	6.5	$0.60^{0.17}_{-0.15}$	11.5	$3.65^{0.49}_{-0.49}$
N2CO_1_23	N2CO J100021+020041	150.0887	2.0115	10.8	$1.26^{0.22}_{-0.20}$	11.0	$4.47^{0.63}_{-0.59}$
N2CO_1_24	N2CO J100029+020527	150.1205	2.0901	7.9	$0.75^{0.17}_{-0.16}$	11.0	$3.54^{0.49}_{-0.47}$
N2CO_1_25	N2CO J100013+023428	150.0556	2.5736	9.6	$1.14^{0.21}_{-0.19}$	10.8	$4.34^{0.60}_{-0.59}$
N2CO_1_26	N2CO J100025+021847	150.1039	2.3127	5.2	$0.47^{0.19}_{-0.14}$	10.8	$3.46^{0.53}_{-0.53}$
N2CO_1_28	N2CO J100104+022858	150.2712	2.4822	5.9	$0.57^{0.18}_{-0.16}$	10.6	$3.52^{0.54}_{-0.54}$
N2CO_1_29	N2CO J095931+023044	149.8826	2.5129	10.1	$1.40^{0.26}_{-0.23}$	10.6	$4.81^{0.80}_{-0.77}$
N2CO_1_30	N2CO J100023+022155	150.0984	2.3647	6.4	$0.61^{0.17}_{-0.15}$	10.4	$3.42^{0.55}_{-0.51}$
N2CO_1_31	N2CO J100020+023520	150.0855	2.5894	6.2	$0.83^{0.24}_{-0.20}$	10.2	$4.71^{0.73}_{-0.71}$
N2CO_1_32	N2CO J100025+020313	150.1061	2.0544	5.8	$0.56^{0.17}_{-0.15}$	10.2	$3.31^{0.53}_{-0.50}$
N2CO_1_33	N2CO J100114+022705	150.3109	2.4502	6.7	$0.64^{0.18}_{-0.15}$	10.1	$3.30^{0.52}_{-0.52}$
N2CO_1_34	N2CO J100049+022258	150.2079	2.3834	7.2	$0.68^{0.16}_{-0.15}$	10.0	$3.37^{0.53}_{-0.53}$
N2CO_1_35	N2CO J100059+021716	150.2462	2.2874	5.8	$0.55^{0.17}_{-0.15}$	9.8	$3.14^{0.53}_{-0.48}$
N2CO_1_36	N2CO J100015+022445	150.0660	2.4127	5.2	$0.50^{0.16}_{-0.14}$	9.8	$3.18^{0.50}_{-0.50}$
N2CO_1_39	N2CO J100007+021148	150.0321	2.1970	6.6	$0.64^{0.17}_{-0.15}$	9.5	$3.15^{0.50}_{-0.51}$
N2CO_1_40	N2CO J100008+021306	150.0362	2.2191	5.3	$0.52^{0.16}_{-0.15}$	9.5	$3.09^{0.50}_{-0.49}$
N2CO_1_41[a]	N2CO J100027+023137	150.1118	2.5252	9.2	$0.86^{0.16}_{-0.15}$	9.2	$3.41^{0.59}_{-0.54}$
N2CO_1_42	N2CO J100111+022841	150.2982	2.4780	6.9	$0.68^{0.18}_{-0.16}$	9.2	$3.16^{0.58}_{-0.51}$
N2CO_1_45	N2CO J100025+020051	150.1059	2.0143	7.7	$0.90^{0.20}_{-0.19}$	9.2	$3.74^{0.68}_{-0.62}$
N2CO_1_46	N2CO J100054+023435	150.2275	2.5768	6.6	$0.81^{0.21}_{-0.19}$	9.1	$3.79^{0.67}_{-0.62}$
N2CO_1_47	N2CO J100102+022236	150.2591	2.3771	6.5	$0.61^{0.17}_{-0.15}$	9.1	$2.96^{0.52}_{-0.48}$
N2CO_1_49	N2CO J100026+021528	150.1098	2.2576	6.7	$0.63^{0.18}_{-0.15}$	9.0	$3.01^{0.54}_{-0.50}$
N2CO_1_50	N2CO J100012+020124	150.0524	2.0243	8.2	$0.87^{0.18}_{-0.17}$	9.0	$3.38^{0.62}_{-0.56}$
N2CO_1_51	N2CO J100024+022005	150.1015	2.3352	5.1	$0.47^{0.18}_{-0.14}$	8.9	$2.90^{0.54}_{-0.47}$
N2CO_1_53	N2CO J100104+020203	150.2685	2.0338	5.1	$0.50^{0.19}_{-0.15}$	8.6	$3.00^{0.55}_{-0.51}$
N2CO_1_54	N2CO J095952+022139	149.9690	2.3599	4.8	$0.44^{0.18}_{-0.14}$	8.6	$2.73^{0.52}_{-0.47}$
N2CO_1_55	N2CO J100047+021016	150.1966	2.1708	5.6	$0.53^{0.16}_{-0.14}$	8.4	$2.82^{0.53}_{-0.48}$
N2CO_1_58	N2CO J100047+020938	150.1967	2.1604	8.5	$0.77^{0.15}_{-0.15}$	8.4	$2.66^{0.50}_{-0.46}$
N2CO_1_59	N2CO J100105+022132	150.2730	2.3592	5.4	$0.36^{0.13}_{-0.12}$	8.3	$2.65^{0.51}_{-0.46}$

Notes. The first and second columns are the N2CLS short names and the IAU names, respectively. The R.A.$_{2\,mm}$ and Dec$_{2\,mm}$ columns are the coordinates of the sources measured in the 2 mm maps. The four last columns (S/N$_{2\,mm}$, S$_{2\,mm}$, S/N$_{1.2\,mm}$ et S$_{1.2\,mm}$) are the S/N at 2 mm, the N2CLS flux at 2 mm, the S/N at 1.2 mm, and the N2CLS flux at 1.2 mm, respectively. For the source without 1.2 mm counterpart, we provide a 5 σ upper limit on the flux. The redshifts are provided in Berta et al. (2025).

[a] These 2 mm sources have two 1.2 mm counterparts. In our analysis, we use the sum of the two 1.2 mm sources to compute their color. The uncertainties are combined quadratically.

Table B.3. Continued.

N2CLS name	IAU name	R.A.$_{2\,mm}$ deg	Dec$_{2\,mm}$ deg	S/N$_{2\,mm}$	S$_{2\,mm}$ mJy	S/N$_{1.2\,mm}$	S$_{1.2\,mm}$ mJy
N2CO_1_60	N2CO J100010+022223	150.0424	2.3737	5.3	$0.51^{0.16}_{-0.14}$	8.3	$2.68^{0.50}_{-0.46}$
N2CO_1_62	N2CO J100012+021211	150.0544	2.2029	5.9	$0.55^{0.17}_{-0.15}$	8.3	$2.71^{0.52}_{-0.46}$
N2CO_1_63	N2CO J095950+022827	149.9610	2.4743	4.9	$0.44^{0.18}_{-0.14}$	8.3	$2.62^{0.51}_{-0.44}$
N2CO_1_65	N2CO J100112+020852	150.3008	2.1477	8.5	$0.86^{0.16}_{-0.17}$	8.2	$2.85^{0.55}_{-0.49}$
N2CO_1_67	N2CO J095953+021853	149.9721	2.3147	7.8	$0.72^{0.16}_{-0.15}$	8.0	$2.58^{0.54}_{-0.51}$
N2CO_1_71	N2CO J100104+022634	150.2693	2.4427	4.7	$0.43^{0.17}_{-0.14}$	7.8	$2.58^{0.54}_{-0.49}$
N2CO_1_72	N2CO J100024+022947	150.1001	2.4962	7.0	$0.65^{0.15}_{-0.14}$	7.7	$2.53^{0.54}_{-0.49}$
N2CO_1_74	N2CO J100057+021309	150.2393	2.2193	6.7	$0.63^{0.17}_{-0.15}$	7.7	$2.50^{0.53}_{-0.48}$
N2CO_1_76	N2CO J100105+022151	150.2718	2.3631	5.4	$0.34^{0.14}_{-0.11}$	7.7	$2.41^{0.51}_{-0.47}$
N2CO_1_78	N2CO J100117+023218	150.3230	2.5378	6.0	$0.64^{0.19}_{-0.17}$	7.6	$2.73^{0.59}_{-0.52}$
N2CO_1_79	N2CO J100058+020138	150.2436	2.0285	6.1	$0.62^{0.17}_{-0.15}$	7.5	$2.72^{0.57}_{-0.53}$
N2CO_1_85	N2CO J100041+022547	150.1749	2.4291	4.6	$0.42^{0.17}_{-0.14}$	7.4	$2.37^{0.53}_{-0.46}$
N2CO_1_87	N2CO J100109+021727	150.2907	2.2897	4.8	$0.44^{0.17}_{-0.14}$	7.3	$2.35^{0.52}_{-0.46}$
N2CO_1_88	N2CO J100056+020842	150.2342	2.1450	5.2	$0.49^{0.18}_{-0.15}$	7.3	$2.37^{0.52}_{-0.47}$
N2CO_1_93	N2CO J100106+021532	150.2783	2.2587	5.2	$0.50^{0.19}_{-0.15}$	7.2	$2.45^{0.54}_{-0.48}$
N2CO_1_97	N2CO J100013+020902	150.0534	2.1495	5.9	$0.57^{0.18}_{-0.15}$	7.1	$2.39^{0.52}_{-0.48}$
N2CO_1_99	N2CO J100118+022352	150.3279	2.3980	4.8	$0.51^{0.20}_{-0.16}$	7.0	$2.56^{0.55}_{-0.52}$
N2CO_1_101	N2CO J100046+021309	150.1923	2.2197	7.9	$0.75^{0.17}_{-0.16}$	6.9	$2.25^{0.57}_{-0.51}$
N2CO_1_108	N2CO J095944+022109	149.9344	2.3530	7.0	$0.68^{0.18}_{-0.16}$	6.6	$2.23^{0.57}_{-0.51}$
N2CO_1_111	N2CO J100018+021241	150.0769	2.2107	4.8	$0.45^{0.18}_{-0.14}$	6.6	$2.21^{0.56}_{-0.49}$
N2CO_1_114	N2CO J100103+022140	150.2639	2.3616	6.3	$0.56^{0.16}_{-0.14}$	6.5	$2.07^{0.55}_{-0.48}$
N2CO_1_118	N2CO J100035+022827	150.1477	2.4740	6.1	$0.57^{0.17}_{-0.14}$	6.4	$2.04^{0.53}_{-0.46}$
N2CO_1_128	N2CO J100048+023016	150.2042	2.5033	6.1	$0.57^{0.16}_{-0.14}$	6.2	$1.71^{0.50}_{-0.45}$
N2CO_1_138	N2CO J095958+020604	149.9915	2.0998	5.2	$0.49^{0.18}_{-0.15}$	5.9	$1.98^{0.59}_{-0.50}$
N2CO_1_143	N2CO J095948+022752	149.9546	2.4641	5.7	$0.54^{0.16}_{-0.15}$	5.9	$1.94^{0.59}_{-0.50}$
N2CO_1_156	N2CO J100105+023239	150.2741	2.5447	4.7	$0.46^{0.18}_{-0.14}$	5.6	$1.89^{0.57}_{-0.50}$
N2CO_1_166	N2CO J100015+020531	150.0630	2.0921	6.6	$0.61^{0.17}_{-0.15}$	5.4	$1.72^{0.56}_{-0.45}$
N2CO_1_167	N2CO J100006+023306	150.0281	2.5519	4.8	$0.48^{0.19}_{-0.15}$	5.4	$1.90^{0.60}_{-0.51}$
N2CO_1_170	N2CO J100057+021347	150.2373	2.2284	5.0	$0.46^{0.18}_{-0.14}$	5.3	$1.71^{0.54}_{-0.46}$
N2CO_1_204	N2CO J100119+022617	150.3303	2.4385	4.7	$0.50^{0.20}_{-0.16}$	4.8	$1.81^{0.67}_{-0.55}$
N2CO_1_208	N2CO J100027+023344	150.1166	2.5632	5.2	$0.54^{0.21}_{-0.17}$	4.8	$1.67^{0.62}_{-0.52}$
N2CO_2_29[b]	N2CO J100001+022819	150.0083	2.4721	7.1	$0.67^{0.15}_{-0.14}$	–	–
N2CO_2_37	N2CO J100114+020208	150.3123	2.0356	6.6	$0.71^{0.20}_{-0.17}$	–	<2.71
N2CO_2_44	N2CO J095945+023438	149.9380	2.5773	6.3	$0.79^{0.22}_{-0.19}$	–	<2.92
N2CO_2_49	N2CO J100100+020923	150.2523	2.1566	6.1	$0.57^{0.16}_{-0.14}$	–	<2.68
N2CO_2_61[b]	N2CO J095952+020544	149.9671	2.0957	5.5	$0.53^{0.16}_{-0.14}$	–	–
N2CO_2_76	N2CO J100042+020739	150.1759	2.1276	4.9	$0.46^{0.18}_{-0.15}$	–	<2.24
N2CO_2_77	N2CO J095953+020734	149.9735	2.1261	4.9	$0.45^{0.18}_{-0.14}$	–	<3.17
N2CO_2_85	N2CO J100059+022603	150.2489	2.4343	4.7	$0.43^{0.17}_{-0.14}$	–	<2.82
N2CO_2_88	N2CO J100050+022953	150.2103	2.4983	4.6	$0.41^{0.17}_{-0.13}$	–	<2.51
N2CO_2_90	N2CO J095944+022227	149.9346	2.3744	4.6	$0.45^{0.18}_{-0.15}$	–	<3.10

Notes. [(b)] These two 2-mm sources are complex blends with a slightly-offset bright 1.2 mm counterpart and potentially a fainter emission coming from the 2 mm object (see Carvajal- Bohorquez et al. in prep.). For this reason, we cannot provide an upper limit on their 1.2 mm flux.